Geophysical Journal International

The static and time-dependent signature of ocean–continent and ocean–ocean subduction: the case studies of Sumatra and Mariana complexes

A.M. Marotta ⬤, F. Restelli, A. Bollino, A. Regorda ⬤ and R. Sabadini

Department of Earth Sciences 'A. Desio', Universitá degli Studi di Milano, L. Mangiagalli 34, Milano 20134, Italy. E-mail: anna.maria.marotta@unimi.it

SUMMARY

The anomalous density structure at subduction zones, both in the wedge and in the upper mantle, is analysed to shed light on the processes that are responsible for the characteristic gravity fingerprints of two types of subduction: ocean–continent and ocean–ocean. Our modelling is then performed within the frame of the EIGEN-6C4 gravitational disturbance pattern of two subductions representative of the above two types, the Sumatra and Mariana complexes, finally enabling the different characteristics of the two patterns to be observed and understood on a physical basis, including some small-scale details. A 2-D viscous modelling perpendicular to the trench accounts for the effects on the gravity pattern caused by a wide range of parameters in terms of convergence velocity, subduction dip angle and lateral variability of the crustal thickness of the overriding plate, as well as compositional differentiation, phase changes and hydration of the mantle. Plate coupling, modelled within a new scheme where the relative velocity at the plate contact results self-consistently from the thermomechanical evolution of the system, is shown to have an important impact on the gravity signature. Beyond the already understood general bipolar fingerprint of subduction, perpendicular to the trench, we obtain the density and gravity signatures of the processes occurring within the wedge and mantle that are responsible for the two different gravity patterns. To be compliant with the geodetic EIGEN-6C4 gravitational disturbance and to compare our predictions with the gravity at Sumatra and Mariana, we define a *model normal Earth*. Although the peak-to-peak gravitational disturbance is comparable for the two types of subductions, approximately 250 mGal, from both observations and modelling, encompassing the highest positive maximum on the overriding plates and the negative minimum on the trench, the trough is wider for the ocean–ocean subduction: approximately 300 km compared to approximately 180 km for the ocean–continent subduction. Furthermore, the gravitational disturbance pattern is more symmetric for the ocean–ocean subduction compared to the ocean–continent subduction in terms of the amplitudes of the two positive maxima over the overriding and subducting plates. Their difference is, for the ocean–ocean type, approximately one half of the ocean–continent one. These different characteristics of the two types of subductions are exploited herein in terms of the different crustal thicknesses of the overriding plate and of the different dynamics in the wedge and in the mantle for the two types of subduction, in close agreement with the gravity data.

Key words: Numerical modelling; Gravity anomalies and Earth structure; Subduction zone processes; Asia.

1 INTRODUCTION

In subduction zones, various processes are responsible for the development of density anomalies, whose characteristic lengths, both horizontally and vertically, cover a wide spectrum of wavelengths due to the complexity of the interaction between the subducting and overriding plates.
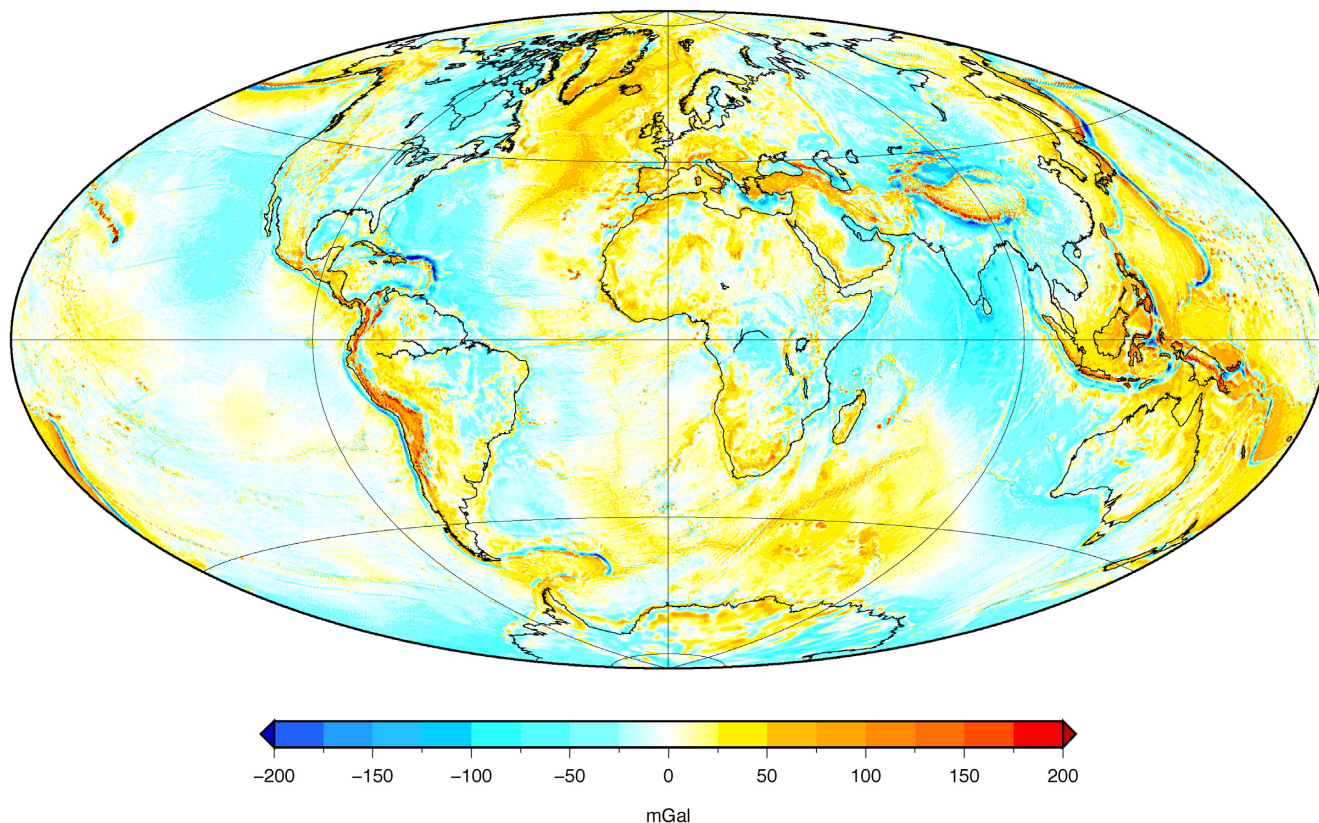
Figure 1. Global map of the gravitational disturbance computed at a height $h_S = 5$ km above the ellipsoid based on the EIGEN-6C4 model (the latest combined static global gravity field model including GOCE data up to degree and order 2190, Förste *et al.* 2014).

In turn, these density anomalies are responsible for characteristic gravity patterns, representing the fingerprint of the dynamic processes involving the crust and the mantle. The gravitational signal at subduction zones is generally characterized by a low-intensity positive anomaly from the trench towards the ocean, a deep negative anomaly in the vicinity of the trench, and a more intense positive anomaly, often composed of several peaks, towards the upper plate (Fig. 1).

The positive anomaly towards the ocean, which is extended but not very intense, is called the *outer gravity high* (Watts & Talwani 1974) and is due to the external rise of the trench, called *bulge*. This anomaly is generally accompanied by a regional topographical rise.

Similar to the first positive peak, the negative anomaly in the vicinity of the trench primarily reflects topographical depression at the oceanic trench. An extended positive anomaly is also observed above the upper plate, superimposed by a narrower (100–150 km) and higher positive anomaly (>100 mGal), which in the ocean–ocean context coincides with the island arcs. This anomaly reflects the combination of the topography and dynamics of the backarc area (Bassett & Watts 2015a,b).

A series of pioneering works (Hager 1984; Gurnis & Hager 1988; Zhong & Gurnis 1992) are the pillars of our understanding of the dynamics of subduction processes and thus of the long-wavelength geoid, gravity and topography anomalies. Melosh & Raefsky (1980) demonstrated that positive and negative pressure anomalies are induced beneath the trench and island arc of a viscoelastic subducting plate isolated from the surrounding mantle, thus showing that topography and gravity anomalies are dynamically supported at subduction zones. Hager *et al.* (1983) and Gurnis & Hager (1988), embedding the colliding plates within a viscous mantle, successfully interpreted the dip angles and the time-evolution of subducting plates. Zhong & Gurnis (1992) and Zhong & Gurnis (1994) , within the frame of a viscous flow model, highlighted the effects of the subduction fault on the topography and free-air gravity patterns, demonstrating the importance of plate coupling on the trench topography. Compared to the 1980s and 1990s, we now have access to improved gravity models, both static and time-dependent models, thanks to space gravity missions, particularly GOCE (Gravity and steady-state Ocean Circulation Explorer) and GRACE (Gravity Recovery And Climatological Experiment), which allow us to exploit the gravity of our planet to a resolution of approximately 80 km (static) and 300 km (time-dependent), with the perspective of going further by resolving the time-dependent gravity field at the wavelength of the present-day static component (Silvestrin *et al.* 2012). The present work explores the gravity effects of complexities such as compositional stratification of the crust-lithosphere system, mantle hydration, and degree of plate coupling at ocean–continent and ocean–ocean subduction zones within the frame of dynamic self-consistent viscous modelling, which improves our capability to interpret short-wavelength features of the gravity patterns at subduction zones, as currently allowed by modern space gravity missions. Due to the dynamic nature of subduction, we exploit the full time-dependent evolution of the gravity patterns of the subduction processes for both ocean–continent and ocean–ocean subductions, including estimates of their rate of change. The gravity pattern at subduction zones recovered by GOCE, providing homogeneous coverage of the gravity, reflects the present-day density anomaly configuration. The latter is a snapshot taken today of the process that started

at the beginning of collision: the present-day density anomaly distribution, made visible by its gravity fingerprint, must thus be coherent with that resulting today from the entire collision process. From this perspective, Marotta *et al.* (2006) and Marotta *et al.* (2007), within the frame of a newly developed finite-element numerical model, explored the role of the compositional stratification of light crust and dense lithospheric mantle in shaping the bipolarity of the gravity pattern. They showed that the negative gravity anomalies are correlated with the sinking of light crustal material, belonging to the subducting and overriding plates, while the positive anomalies are due to the thermally contracted subducted slab.

Compared with Marotta *et al.* (2006), this study introduces new complexities, such as phase changes, hydration of the mantle and plate coupling, allowing us to provide the most realistic density distribution in the crust–mantle system and the corresponding gravity pattern, currently comparable with updated global gravity models, such as EIGEN-6C4 (Fig. 1). A major issue considered in our analysis is the coupling between the subducting and overriding plates. Although considered in the aforementioned paper by Zhong & Gurnis (1992), we consider the effects of the coupling within the frame of our viscous models where all the other effects, from compositional stratification, hydration and phase changes, are included to provide a realistic and detailed picture of the impact of coupling on the density distribution at depth in the collision zone and its gravity signatures. We expect that gravity can provide hints regarding the amount of plate coupling.

2 MODEL SETUP

The dynamics of the crust and mantle system are governed by the continuity, momentum and energy equations, which can be expressed as follows:

$$\frac{\partial \rho}{\partial t} + \nabla \cdot (\rho \boldsymbol{u}) = 0 \tag{1}$$

$$-\nabla p + \nabla \cdot \boldsymbol{\tau} + \rho \boldsymbol{g} = \boldsymbol{0} \tag{2}$$

$$\rho C_p \left(\frac{\partial T}{\partial t} + \mathbf{u} \cdot \nabla T \right) = \nabla \cdot (K \nabla T) + H, \tag{3}$$

where **u** is the velocity, p is the pressure, $\boldsymbol{\tau}$ is the deviatoric stress, ρ is the density, $\boldsymbol{g}$ is the gravity acceleration, c_p is the heat capacity at constant pressure, T is the temperature, K is the thermal conductivity and H is the total internal heating per mass unit.

Density varies with composition, temperature and pressure. To account for compressibility, we use the extended Boussinesq approximation (Ismail-Zadeh & Tackley 2010, and reference therein), and its implementation is described in detail in Appendix A. Here, we summarize only the main characteristics of this approximation. The balance equations are numerically integrated via the 2-D finite element (FE) thermomechanical code *SubMar* (Marotta *et al.* 2006) in a 2-D 1000 km wide and 700 km deep rectangular domain (Fig. 2a). During the progression of subduction, erosion/sedimentation, mantle hydration/dehydration and phase changes are allowed and implemented as detailed in Appendices A–C. The domain is discretized by a non-deforming irregular grid composed of 6813 quadratic triangular elements and 13 846 nodes, carrying a denser nodal distribution near the contact region between the plates, where the most significant gradients in temperature, pressure and velocity fields are expected. The sizes of the elements vary from 30 to 2.5 km, and the smallest elements are located in proximity to the active margin region to a depth of 300 km.

The marker-in-cell technique has been used to compositionally differentiate different types of materials (e.g. sediment, water, crust and mantle), and at the beginning of the evolution, 455 489 markers are spatially distributed with a density of 1 marker per 0.25 km^2, identifying through a specific index the material particles of air, water, upper and lower oceanic crust, upper and lower continental crust and the mantle belonging to the upper plate. During the evolution of the system, each marker is advected using a 4th-order (both in time and in space) Runge–Kutta scheme. Based on the number and type of markers within each element, at each time it is possible to define the elemental composition and, consequently, all the properties, as specified in eqs (A2)–(A4) of Appendix A. The initial thickness of the oceanic crust is fixed at 10 km, subdivided into a 5-km-thick upper crust and a 5-km-thick lower crust, while the continental crust is 30 km, subdivided into a 20-km-thick upper and a 10-km-thick lower crust. To allow for topographic variations a 7.5-km-thick layer of sticky air has been introduced above the crust. Only in the oceanic part of the domain, a sticky water layer of thickness h_w is sandwiched between the sticky air and the crust (Fig. 2a). When we refer to topography, we do not mean the upper boundary of the model, which does not deform, but the surface defined through the envelope of the topmost continental and/or oceanic crustal markers. Several comparative studies have demonstrated that, when appropriate low density and low viscosity values are considered (as low as 0–1 kg m^{-3} for density and 10^{18}–10^{20} Pa·s for viscosity), by means of the sticky air method the air/crust interface behaves in a manner that is very similar to that of a true free surface (Schmeling *et al.* 2008; Crameri *et al.* 2012; Ruh *et al.* 2013). In this study we assume a value of 10^{18} Pa·s for the air/water viscosity and values of 1 and 1000 kg m^{-3} for the air and water density, respectively.

The model combines a linear viscous rheology for the sublithospheric mantle with a linear viscoplastic rheology for the lithosphere, as detailed in Appendix A.

The initial global thermal configuration of the system corresponds to a conductive gradient throughout the lithosphere, with a temperature that ranges from 300 K at the surface to 1600 K at its base and a uniform temperature of 1600 K below the lithosphere to the bottom of the model. At the beginning of subduction, the base of the thermal lithosphere is fixed at a depth of 80 km under the lower plate and at 80 or 150 km under the upper plate (red solid and dashed lines in panel a of Fig. 2). A thickness of 80 km corresponds to either an oceanic
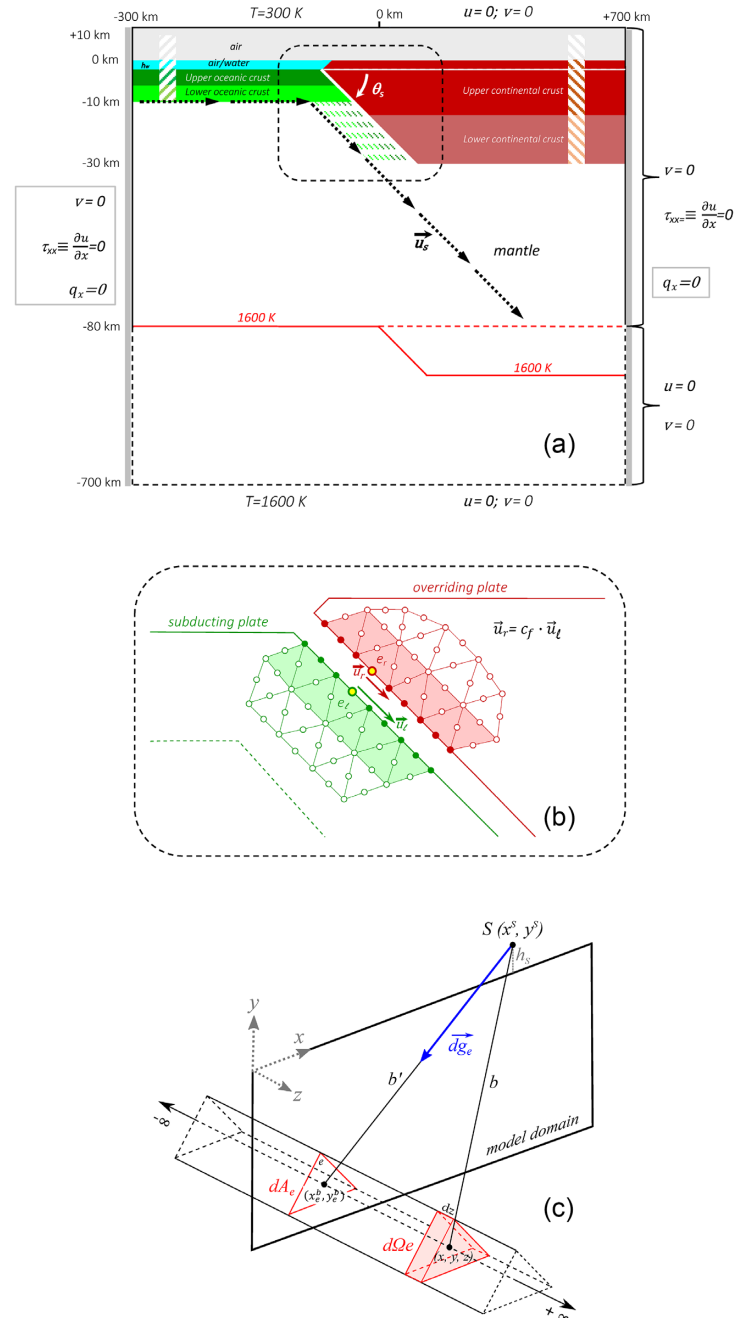
Figure 2. (a) Model setup and boundary conditions. Axes, *x* horizontal and *y* vertical, are not to scale. (b) Scheme used to implement the plate coupling factor. Triangles are representative of the numerical grid used. Red and green colours are used to graphically differentiate the two sides of the decoupling plane. The empty circles indicate the grid nodes. The solid circles indicate the *slip nodes*. (c) Scheme used to compute the volume integrals of eqs (6) and (7). Distances are not to scale.

lithosphere of approximately 40 Myr (Turcotte & Schubert 2002) or to a thinned continental passive margin extending at a medium-to-slow spreading rate of 2–3 cm yr^{-1} (e.g. Marotta *et al.* 2018). The 1600 K isotherm defines the base of the thermal lithosphere throughout the evolution of the system.

We use different type of boundary conditions, either Dirichlet or Neumann type, along different boundary of the 2-D domain (Fig. 2a), where we prescribe values of velocities and temperatures or their normal derivative.

The thermal boundary conditions correspond to fixed temperatures at the upper (300 K) and lower (1600 K) boundaries of the model and to zero thermal flux through the vertical sidewalls. To minimize the potential effects of an unrealistic motion of the two plates with respect to the deep mantle, our model setup is constructed such that the trench is fixed with respect to the bottom of the 2-D convective cell. This assumption, which is also encountered in the perspective of the successive application to the case studies of the Sumatra and Mariana subduction complexes, is consistent with the absolute plate motion by Wang *et al.* (2018) at these two locations.

Table 1. List of the models implemented for the present analysis. U_{cc}/L_{cc}: stratified (yes) or homogeneous (no) continental crust of the upper plate; u_s: prescribed subduction velocity; θ_s: prescribed subduction dip angle; c_f: degree of plate coupling; L_c: initial thickness of the upper plate; h_t: maximum topographic height before the activation of erosion; c_{f_o}: degree of coupling between the subducting plate and the sticky air layer. *ms*: modified sedimentation algorithm.

Model ID	U_{cc}/L_{cc}	u_s (cm yr^{-1})	θ_s (°)	c_f	L_c (km)	h_t (km)	c_{f_o}
Ocean–continent context							
OC_1	No	5	45	1	80	2.5	1
OC_2	Yes	5	45	1	80	2.5	1
OC_3	Yes	5	45	0.5	80	2.5	1
OC_4	Yes	5	45	0.5	80	2.5	0
OC_5	Yes	5	45	0.25	80	2.5	1
OC_6	Yes	8	45	0.5	80	2.5	1
OC_7	Yes	5	60	0.5	80	2.5	1
OC_8	No	5	45	1	150	2.5	1
OC_9	No	5	45	0.5	150	2.5	1
OC_{10}	Yes	5	45	0.5	150	2.5	1
OC_{11}	Yes	5	30	1	80	2.5	1
OC_{12}	Yes	2	45	1	80	2.5	1
OC_{13}	Yes	2	45	0.25	80	2.5	1
OC_{14}	Yes	2	45	0.5	80	2.5	1
Ocean–ocean context							
OO_1	–	5	45	1	80	0.0	1
OO_2	–	5	45	1	80	2.5$_{ms}$	1
OO_3	–	5	45	1	80	0.0	0
OO_4	–	5	45	0.5	80	0.0	1
OO_5	–	5	45	0.5	80	2.5$_{ms}$	1
OO_6	–	5	45	0.5	80	0.0	0
OO_7	–	5	45	0.25	80	0.0	1
OO_8	–	5	45	0.25	80	0.0	0
OO_9	–	4	45	0.25	80	0.0	0
OO_{10}	–	4	60	0.5	80	0.0$_{ms}$	1
OO_{11}	–	4	60	0.5	80	0.0$_{ms}$	0
OO_{12}	–	5	60	0.5	80	0.0$_{ms}$	0
OO_{13}	–	2	60	0.5	80	0.0$_{ms}$	1
OO_{14}	–	5	60	0.5	80	2.5$_{ms}$	1
OO_{15}	–	5	60	1	80	0.0$_{ms}$	1
OO_{16}	–	2	60	1	80	0.25$_{ms}$	1

Moreover, no-slip conditions are assumed along the upper (top of the air/water layer) and lower boundaries of the 2-D domain and along the right vertical side, with the exception of the uppermost 80 km, where zero normal viscous stress is assumed. Zero normal viscous stress is also assumed along the vertical left-hand side (Fig. 2a). To force the subduction of the oceanic lithosphere, a convergence velocity $\mathbf{u}_s$ is prescribed along the bottom of the oceanic crust. Velocities of 2, 4, 5 and 8 cm yr^{-1} have been chosen, which are representative of slow, intermediate and fast subductions, respectively. The same velocity is also imposed along a plane that extends from the base of the oceanic lower crust, behind the trench, to a depth of 80 km, with an angle θ_s of 30°, 45° and 60° (dashed black arrows in panel a of Fig. 2). These dip values allow the development of low-, medium-, high-dip subductions and are based on the compilation by Syracuse & Abers (2006) who averaged the slab dips between 50 and 250 km depth, for all the known subductions. Flow is allowed across the left edge to guarantee that the total mass is conserved in the cell.

Finally, a different plate coupling along the contact plane between the lower and upper plates is implemented, modifying the classical split-node technique (Jungels 1973; Jungels & Frazier 1973) by introducing a plate *coupling factor* c_f that varies from 0 to 1 to indicate a shear-free or a fully coupled contact surface, respectively (Fig. 2b). The details about the implementation of the plate *coupling factor* c_f are presented in Appendix D.

The assumption of a total degree of coupling ($c_f = 1$) corresponds to a condition of continuity in the velocity field through the contact surface between the two interacting plates, that is commonly used in similar studies, even when a low viscosity channel or a weak zone are implemented to ensure the separation between the two plates (e.g. Billen & Hirth 2007; Duretz *et al.* 2011) intrinsically contains the condition of continuity. In our study, instead, we simulate a varying degree of coupling in terms of a discrete structural discontinuity. We assume a reference model that simulates a fully coupled subduction in order to enlighten its effects on the gravitational signature of subduction.

Table 1 lists the models implemented in this study and their main characteristics.

Because we are interested in estimating the perturbation induced on the gravity field only by subduction, for each element e of the numerical grid, at each time we calculate the density anomaly as follows:

$$\Delta\rho_e(t) = \rho_e(t) - \rho_e(t_0), \tag{4}$$

where $\rho_e(t)$ is the density within element e at time t and $\rho_e(t_0)$ is the density within the same element at the beginning of subduction.

The elemental density anomaly $\Delta\rho_e(t)$ computed by eq. (4) are then used to calculate the corresponding gravitational contributions at the observational point S, $\Delta g(S, t)$, as follows:

$$\Delta g(S, t) = \sum_{e=1}^{nelem} \mathrm{d}g_e(S, t) \tag{5}$$

$$\mathrm{d}g_e(S, t) = G \iiint\limits_{\Omega_e} \frac{\Delta\rho_e(t)}{b^2} \mathrm{d}\Omega_e, \tag{6}$$

where G is the universal gravitational constant, 6.67×10^{-11} m³kg⁻¹s⁻²; b is the distance between the observational point S and the centre of the volume element $d\Omega_e$ inside grid element e; Ω_e is the volume of the prism, infinitely extended along the direction perpendicular to the model, whose section coincides with the grid element (Fig. 2c); $nelem$ is the total number of the grid elements. After few mathematical steps eq. (6) becomes

$$\mathrm{d}g_e(S, t) = 2\pi G \iint\limits_{A_e} \frac{\Delta\rho_e(t)}{(x^S - x_e^b)^2 + (y^S - y_e^b)^2} \mathrm{d}A_e, \tag{7}$$

where A_e is the area of the grid element, x_e^b and y_e^b are the coordinate of its barycenter and x^S and y^S are the coordinates of the observational point S.

3 MODEL RESULTS AND DISCUSSION

The description of the results concerns the general thermal state of the system and the dynamics in the wedge area, the density distribution and the gravity changes induced by subduction. First, we illustrate the results of a reference model (OC_2 model in Table 1) (Section 3.1). This model simulates a fully coupled ocean–continent subduction ($c_f = 1$), with a subduction velocity $u_s = 5$ cm yr⁻¹, a subduction dip angle $\theta_S = 45°$. Secondly, we compare the results of models characterized by different parameters in order to enlighten the effects of a variation of the degree of coupling c_f (1, 0.5, 0.25), the subduction dip angle θ_S (45° and 60°), the subduction velocity u_s (2, 4, 5 and 8 cm yr⁻¹) and the environment (ocean–ocean and ocean–continent) (Section 3.2).

3.1 Reference model OC_2

3.1.1 General thermomechanics

The general thermomechanical behavior of the crust–mantle system during subduction has already been extensively described in the literature (e.g. Marotta *et al.* 2007; Billen 2008; Afonso & Zlotnik 2011; Roda *et al.* 2012; Gerya 2015; Regorda *et al.* 2017; Dai *et al.* 2018; Stern & Gerya 2018; Wang *et al.* 2019). Here, we will focus on those aspects that we consider to be related to the gravitational signature and its changes in time, which are the objectives of this work.

Fig. 3 shows the temperature and velocity fields predicted by the reference model OC_2 at different times after the beginning of subduction. The system is characterized by the following:

(i) The sinking of the cold lithosphere into the hot mantle and its progressive steepening at great depths (Fig. 3d);

(ii) A convective flow that is activated above the lower plate during the early stages of subduction (Figs 3a and b) and progressively enlarges with the sinking of the slab (Figs 3c and d);

(iii) The large-scale flow that favours the rising of hot mantle in the wedge area, producing a progressive, but local, thermal thinning of the overriding plate (Figs 3c and d).

Focusing on the mass redistribution shown in Fig. 4, it is also worth highlighting the following:

(i) The subducted crustal material originates either from the lower plate or from the upper plate, from which it is scraped (Fig. 4a);

(ii) The scraping effect is maximum within the first 5 Ma (Figs 4a and b);

(iii) During the early stages of subduction, crustal erosion and thinning are controlled by the mechanical coupling between the interacting plates (Figs 4a and b);

(iv) In the advanced stages of subduction, however, the main role of crustal erosion and thinning is played by the local mantle convective flow in the wedge area (Fig. 4c);

(v) Since the beginning of subduction, a widening of the trench trough occurs until a stationary configuration is reached after a few million years (cyan colour in Fig. 4a);
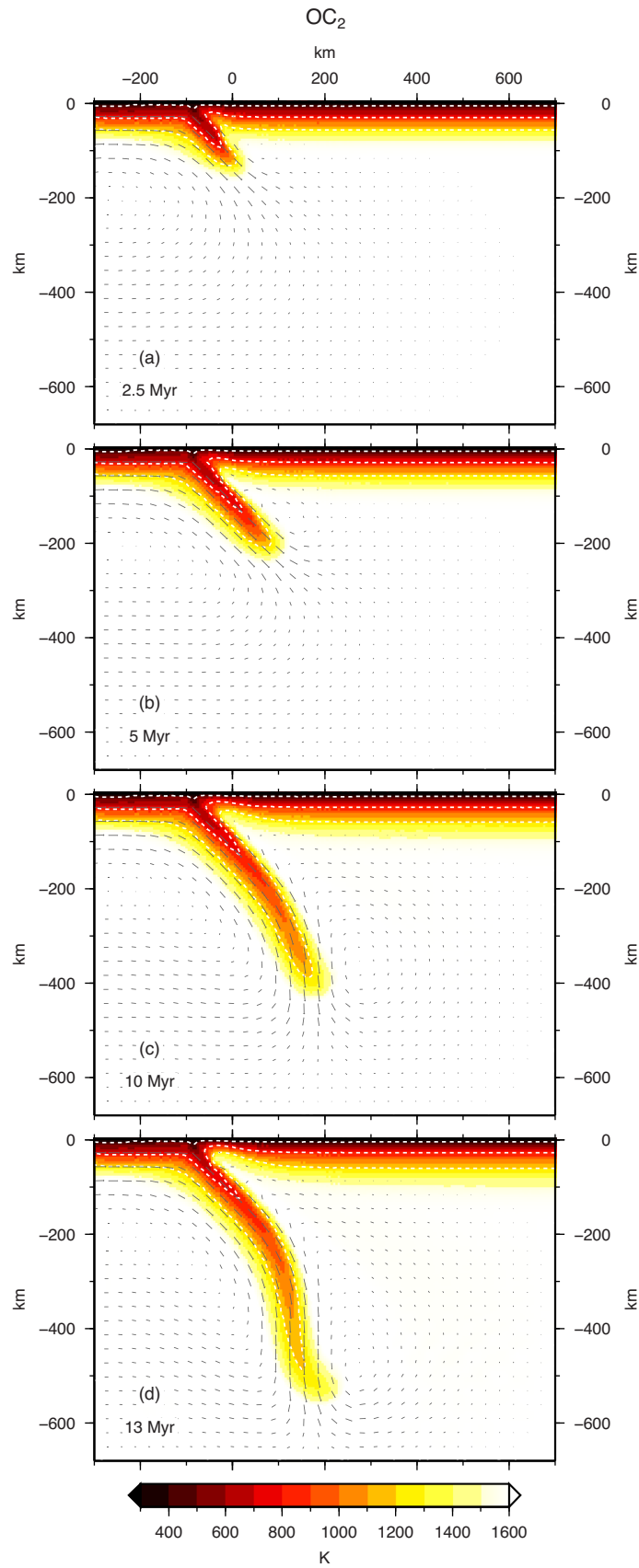
OC$_2$

Figure 3. Large-scale thermal (colour) and velocity (black arrows) fields predicted by the *OC$_2$* model after 2.5 (a), 5 (b), 10 (c) and 13 Myr (d) since the beginning of subduction. The white dashed lines indicate the 400, 800 and 1200 K isotherms. *OC$_2$*: $u_s = 5$ cm yr^{-1}; $\theta_s = 45°$; **c$_f$ = 1**.
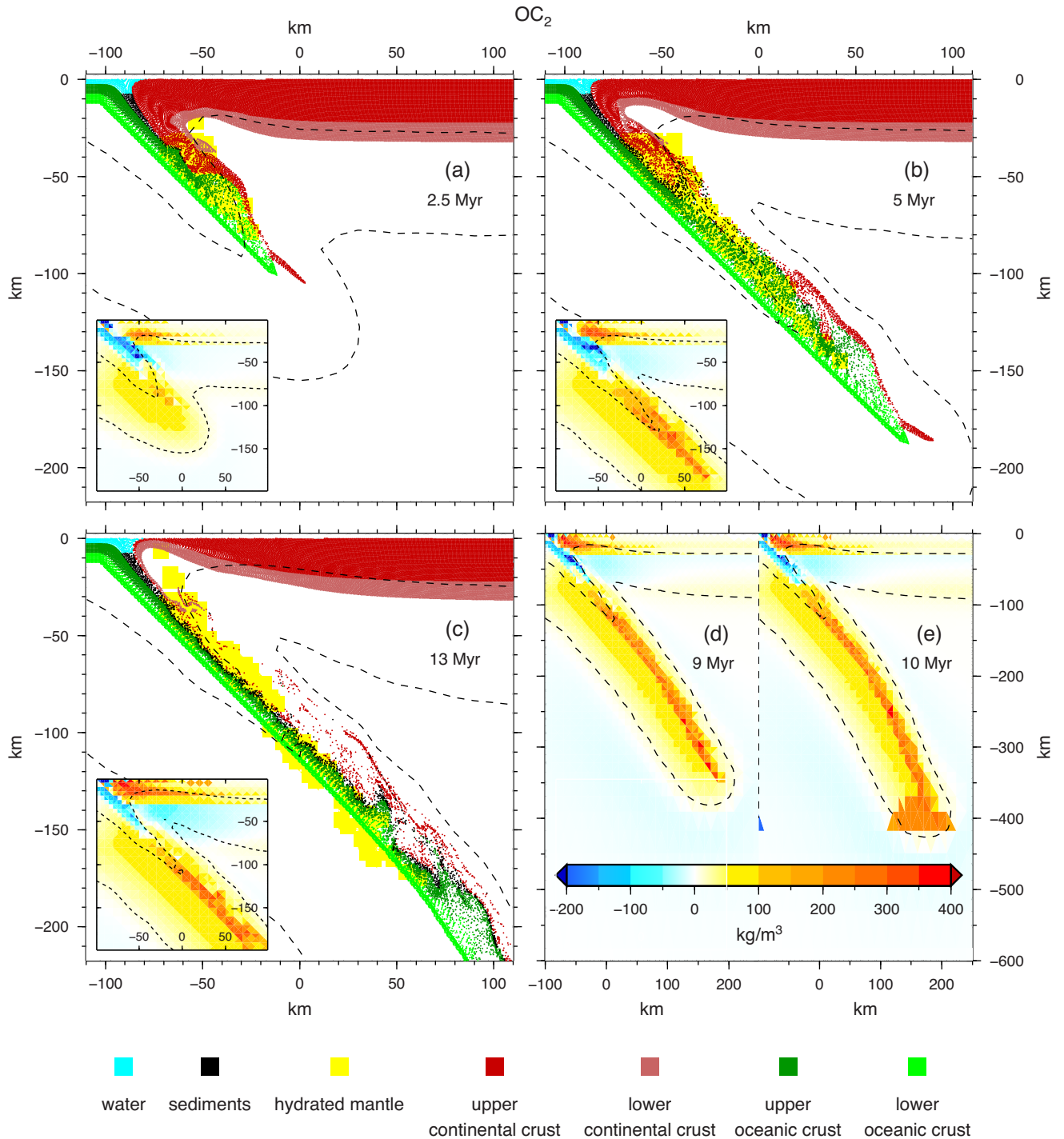
Figure 4. Marker distribution predicted by the OC_2 model after 2.5 (a), 5 (b) and 13 Myr (c) since the beginning of subduction. The insets show the density anomalies at the same times. Panels (d) and (e) show the large-scale density anomaly after 9 (d) and 10 Myr (e). The dashed black lines indicate the 800 and 1500 K isotherms. OC_2: $u_s = 5$ cm yr^{-1}; $\theta_s = 45°$; $c_f = 1$.

(vi) After a few million years, the erosion/sedimentation mechanism is activated, with a vast amount of sediments that, with water, contributes to filling the trench and that sinks to great depths (black dots in Figs 4a–c);

(vii) The p–T conditions become favourable for activating mantle hydration and serpentinization in the wedge area within the first 2 Myr from the beginning of subduction (yellow area in Figs 4a–c).

3.1.2 Density anomalies

The density anomalies predicted by the OC_2 model at different times after the initiation of subduction are shown in the insets of Fig. 4.

Alternating regions of negative (blue colour) and positive (yellow to red colours) density anomalies are localized at shallow depths around the arc-trench region during the whole evolution (insets in Figs 4a–c); a dominant positive density anomaly, increasing in time, characterizes the core of the subducting lithosphere to great depths (Figs 4d and e). Both the extension and the magnitude of the density contrasts are sensitive to the age of subduction.

The negative density anomalies can be attributed to the following:

(i) The negative topography associated with the oceanic trench. The depression that constitutes the oceanic trench is filled with water and sediments and produces the most intense (and shallowest) negative anomalies (insets of Figs 4a–c);

(ii) The light material entrapped in the subduction complex, particularly sediments and slices of continental crust scraped by the upper plate. The sediments and the continental material play a peculiar role: if their presence is initially important (Fig. 4a), then at longer times, their concentration decreases because they are transported at depth by the flow generated by the descent of the subducted plate (Figs 4b and c);

(iii) The hydration of the mantle wedge leading to the development of serpentine (yellow colour in Figs 4a–c) that has a density that is approximately 200 kg m^{-3} lower than that of the non-hydrated mantle;

(iv) The general warming of the system at the mantle levels of the wedge area (see the deflection of the isotherms 800 and 1600 K in Figs 4b and c).

The positive density anomalies can in turn be attributed to the following:

(i) The sinking of cold and dense lithospheric mantle into warm and light material;

(ii) The phase transitions within the subducting plate triggered by the increase in pressure p and temperature T. In fact, mineralogical phases that are stable at lower depths are replaced by denser phases that are stable at higher p–T conditions. The effect of phase transitions adds to the thermal contraction;

(iii) The mantle that rises and fills the space previously occupied by the crust that has been scraped from the overriding plate (Figs 4a–c);

(iv) The general cooling and thermal contraction of the system far away from the trench.

3.1.3 Gravitational contribution

The profiles of the gravitational contributions, calculated for the OC_2 model using eqs (5) and (6), at time intervals of 1 Myr since the beginning of subduction and along the top boundary of the model domain are shown in panel a of Fig. 5. Each profile is characterized by two maxima and a minimum within a distance of 200 km (Fig. 5a). The most intense maximum is located on the upper plate, while the secondary one is located behind the trench. The local minimum is positioned approximatively above the trench. The gravity anomalies decrease progressively outwards, assuming an almost constant value in the far field. With the progression of the subduction, the intensity of the gravity anomalies increases globally, accompanied by a coeval increase in the difference between the absolute maximum and the minimum. For the OC_2 model, the positions of the two maxima and of the minimum remain almost unchanged for the entire evolution.

The analysis of the separate contributions of the positive and negative density anomalies (Figs 5b and c, respectively) allows us to clarify the origin of the peculiar style of the gravitational contribution and its variation in time and space. The bulk of the gravity change due to the negative anomalies in the surrounding of the trench occurs within the first two million years (Fig. 5c) and is attributable to the formation of the trench trough, to the subduction of crust and sediments and to the mantle wedge hydration. Subsequently, the most significant changes occur far from the subduction complex, and these changes can be associated with the progressive but widespread cooling of the system. Conversely, the progressive growth of the positive density anomalies (Fig. 4) induces an equally continuous increase in their gravitational contribution, although with different rates (Fig. 5b). The following four phases in the time variation of the gravity contribution can be distinguished:

(i) A first phase, from the beginning of subduction to approximately 5 Myr. This phase is characterized by the highest rate of growth in the surroundings of the trench, with a total variation of approximately 200 mGal (blue lines in Fig. 5a). During this first period, the subducted slab reaches a depth of more than 200 km (Fig. 3b), and most of the negative and positive density anomalies are localized at shallow/intermediate depths around the trench (inset of Fig. 4b);

(ii) A second phase, from 5 to 9 Myr (cyan to yellow lines in Fig. 5a). During this phase, the gravitational contribution continues to increase, but at a lower rate, and the positive density anomalies still grow but at great depths (Fig. 3c, and inset of Fig. 4c);

(iii) A third phase, from 9 to approximately 11 Myr (yellow to dark orange lines in Fig. 5, panel a). This phase is characterized by a gravity change of approximately 60 mGal within just 2 Myr. Note that this effect occurs when the subducted slab crosses the *olivine* − *spinel* transition at a depth of 410 km (Fig. 4, panels d and e), where a density change of approximately 100 kg m^{-3} occurs. The great depth at which the density variation occurs makes the corresponding perturbation induced on the gravity field have a regional character;

(iv) A fourth phase, from 11 Myr onwards (dark orange to pink lines in Fig. 5a), during which the growth rate is stabilized everywhere at low values of the far field.

Fig. 6 shows the rate of change of the gravitational contribution of the density anomalies predicted by the OC_2 model. The plotted rate of change corresponds to the average value calculated over a time span of 0.5 Myr, which confirms that during the first phase, the
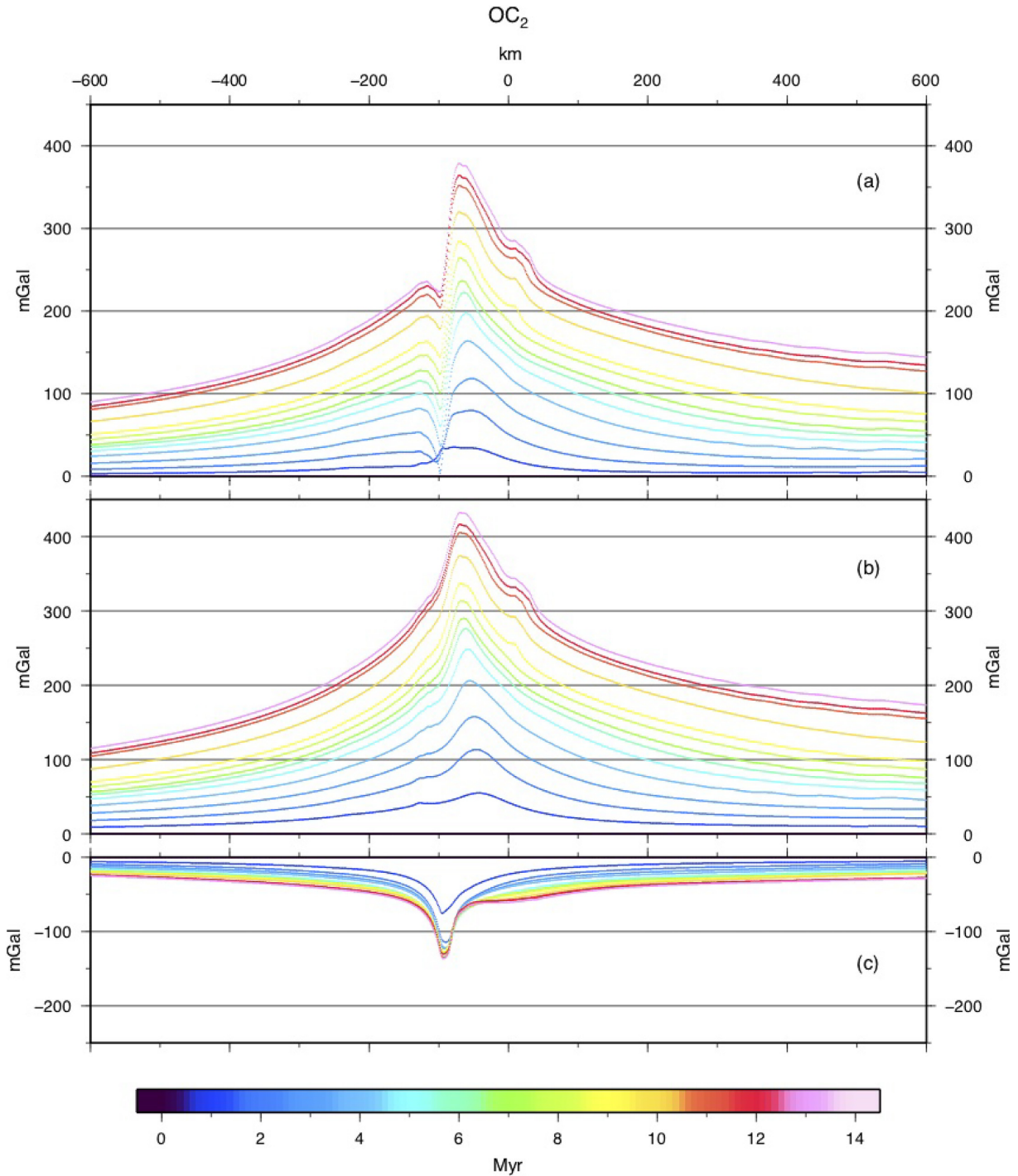
Figure 5. (a) Gravitational contribution of the density anomalies predicted by the OC_2 model after different time intervals since the beginning of subduction. (b) Gravitational contribution of the sole positive density anomalies. (c) Gravitational contribution of the sole negative density anomalies. The profiles are plotted at 1 Myr time intervals. Colours indicate the age of subduction. OC_2: $u_s = 5$ cm yr^{-1}; $\theta_s = 45°$; $c_f = 1$.

gravitational contribution of the negative density anomalies increases rapidly at a rate as high as 0.05 μGal yr^{-1} (Fig. 6c). Afterwards, the rate of change remains smaller than 0.01 μGal yr^{-1}. Regarding the gravitational contribution of the positive density anomalies (Fig. 6b) during the first phase, the corresponding rate of change is comparable to that associated with the negative density anomalies and is reduced by almost a factor of two during the second phase. The discontinuity observed at approximately 9 Myr from the beginning of subduction (yellow lines in Figs 6a and b) is evident here in terms of a rate of change varying from approximately 0.02–0.03 μGal yr^{-1}, moving from the lower to the upper plates; values close to 0.04 μGal yr^{-1} characterize the surroundings of the trench (Figs 6a and b). The low values of the rate of change characterizing the mature phases indicate that, at long times, the contribution from the positive density anomalies becomes quasi-stationary.
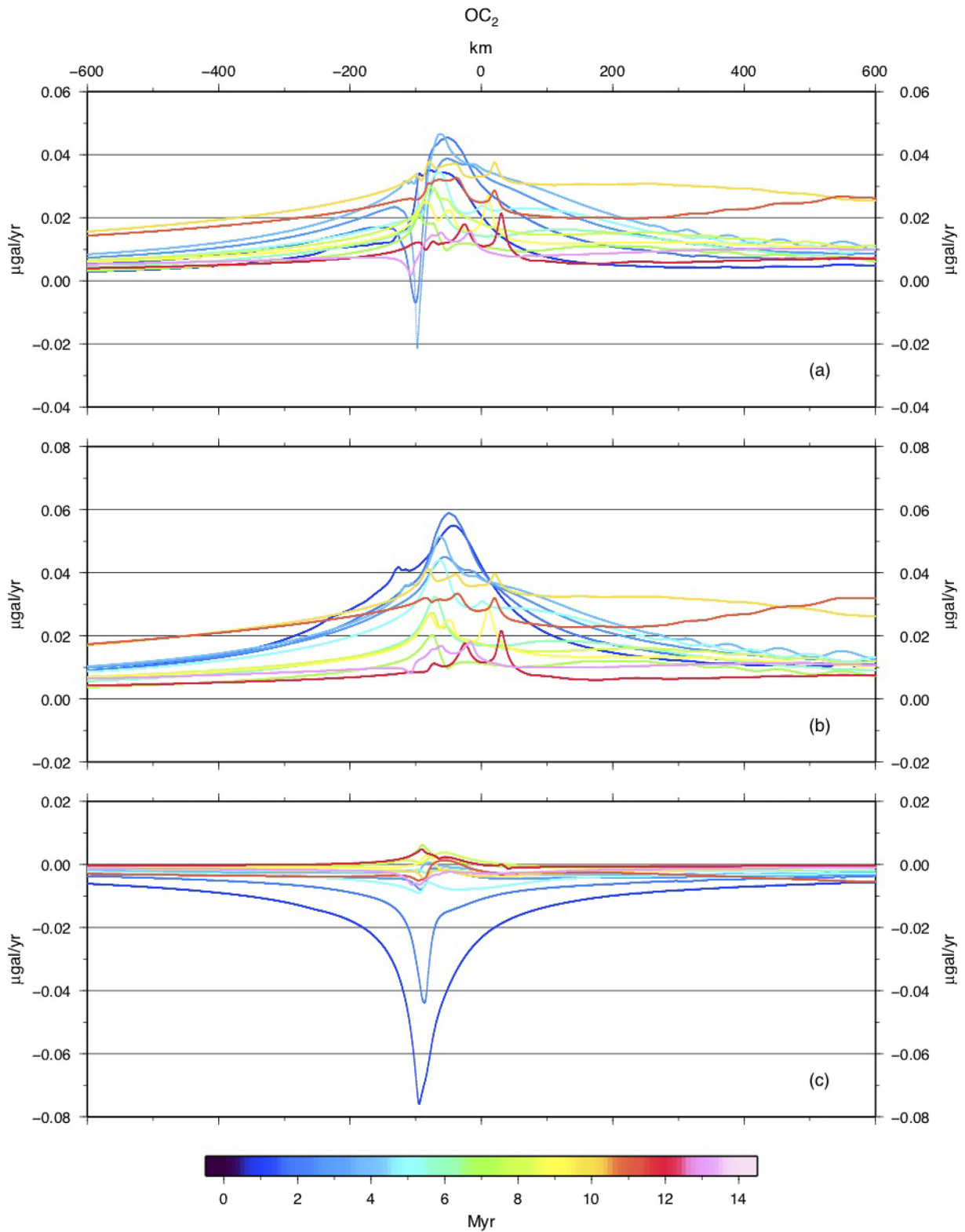
Figure 6. (a) Rate of change of the gravitational contribution of the density anomalies predicted by the OC_2 model after different time intervals since the beginning of subduction. (b) Rate of change of the gravitational contribution of the sole positive density anomalies. (c) Rate of change of the gravitational contribution of the sole negative density anomalies. The profiles are plotted at 1 Myr time intervals. Colours indicate the age of subduction. OC_2: $u_s = 5$ cm yr^{-1}; $\theta_s = 45°$; $c_f = 1$.

3.2 Effects of a varying c_f, θ_S, u_s and of a OO environment

3.2.1 Coupling factor c_f

To investigate the effects of a different degree of plate coupling on the gravitational field, we implemented a different set of models with the same values for all the characteristic parameters, with the exception of the value of the coupling factor c_f, set equal to 1 (total coupled system), 0.5 and 0.25 (almost completely decoupled system). Fig. 7 shows how a different plate coupling degree along the contact between the subducting and overriding plates impacts the global thermomechanics of the subduction complex, with panels a and b corresponding to the fully coupled OC_2 model and panels c and d corresponding to the OC_5 model, characterized by a $c_f = 0.25$. During the early stages of subduction, no significant differences in the global thermal field are evident, with the exception of the slightly lower temperatures in the wedge area occurring as the plate coupling decreases (compare panel c to panel a of Fig. 7). Over time, the difference in the thermal state is intensified and, as the plate coupling decreases, the cooling of the wedge area progressively increases (compare panel d to panel b of Fig. 7) while, at great depths, the subducted slab remains warmer (compare panels e and f of Fig. 7, corresponding to $c_f = 0.25$, to panels c and d of Fig. 3, corresponding to $c_f = 1$). The thermomechanics remain unchanged at great distances from the trench.

The explanation of the enlightened changes in the thermal field stands on the more vigorous small-scale convection when the plate coupling is higher in the corner region between the subducting and overriding plate, which enhances the entering of cold material into the mantle due to the active subduction, making the fully coupled OC_2 model colder at depth compared to the decoupled OC_5 model. At the same time, as already stated in Section 3.1.1, the large-scale flow favours the rising of hot mantle in the wedge area, producing a progressive local thermal thinning of the overriding plate (Figs 3c and d). The concomitance of these two factors makes the system warmer at shallow depths and colder at deep depths. For low coupling (Figs 7c–f) the two plates are partially or totally mechanically disjoined and the low intensity convective cornel flow is not able to perturb the thermal field in the wedge area, where the thermal state becomes increasingly depressed over time. At the same time, the progressive cooling of the wedge area further inhibits the convective flow in the wedge which in turn disfavors the subduction of cold material for the lower plate coupling model, which thus remains warmer at great depths.

The role of plate coupling appears to be even more evident from the distribution of the markers in the wedge area (Fig. 8). At the early stages of subduction, the scraping of the crustal material belonging to the upper plate is increasingly less effective as the plate coupling decreases (Figs 8a and b, compared to Fig. 4a). A smaller amount of the scraped crust is subducted at great depths over time compared to the OC_2 model (Fig. 4c), and over long times, the recycling flow of crustal material inside the hydrated mantle wedge is more intense (Figs 8c and d). Focusing on this last aspect, the maximum depth of the hydrated area is greater for strong plate coupling (Fig. 4 with respect to Fig. 8); conversely, the horizontal extension of the hydrated area increases as the coupling decreases, favoured by the low temperatures that characterize the wedge area.

The differences in the density anomalies predicted by models characterized by different couplings (insets of Fig. 8) increase with the age of subduction. The main differences occur at low depths, where the less effective mantle wedging occurring for low plate coupling causes a shallow positive density anomaly of smaller intensity (insets of Fig. 8 compared to insets of Fig. 4). The positive density anomaly is instead mainly due to the ascent to low depths of the lower crust, which is heavier than the upper crust. The negative density anomaly, associated with the trench trough, the subducted crust and sediments and the mantle hydration, increases and widens laterally as the plate coupling decreases (Figs 8c and d, compared to Fig. 4c). Finally, the diffuse negative density anomaly associated with the warming of the mantle in the wedge area disappears for low values of plate coupling.

Fig. 9 shows the gravitational contribution predicted by the OC_3 and OC_5 models, accounting for plate couplings of $c_f = 0.5$ and $c_f = 0.25$, respectively. The decrease in the maximum value of the positive contribution accompanying the decrease in plate coupling is due to both the warming of the internal part of the subducted plate, which is lighter for low plate coupling with respect to the strong coupling (Figs 7e and f), and to the missing wedging mantle flow (Figs 8b and d). In contrast, the gravitational contribution due to negative density anomalies increases both in magnitude and in width as the plate coupling decreases, reflecting the differences in the negative density anomaly distribution discussed above and particularly the progressive enlargement of the hydrated mantle area where a very intense recirculation of crustal material occurs (Figs 8b and d).

Note that with the progression of the subduction, the amplitude of the gravity trough increases as the plate coupling decreases. Although the degree of plate coupling does not affect the position of the local minimum that remains localized above the trench throughout the evolution, the position of the absolute maximum moves forward over the upper plate as the degree of plate coupling decreases (Fig. 9), which is correlated with the main role played by the heavy subducted slab in localizing the bulk of the positive density anomaly further away from the trench, below the upper plate, as subduction progresses.

3.2.2 Subduction dip θ_S

Fig. 10 shows the temperature and velocity fields (panels a and b), the marker distribution (panels c and d) and the density anomalies (insets of panels c and d) predicted after 2.5 and 13 Myr from the beginning of subduction by the OC_7 model that is characterized by a subduction velocity $u_s = 5 \, \text{cm yr}^{-1}$, a coupling factor $c_f = 0.5$ and a subduction dip $\theta_s = 60°$.

With respect to the homologous 45° OC_3 model, a higher subduction dip angle allows the development of a more intense mantle wedge flow, responsible for a stronger erosion and thinning of the upper plate, with a larger amount of light material (both crust and sediments)
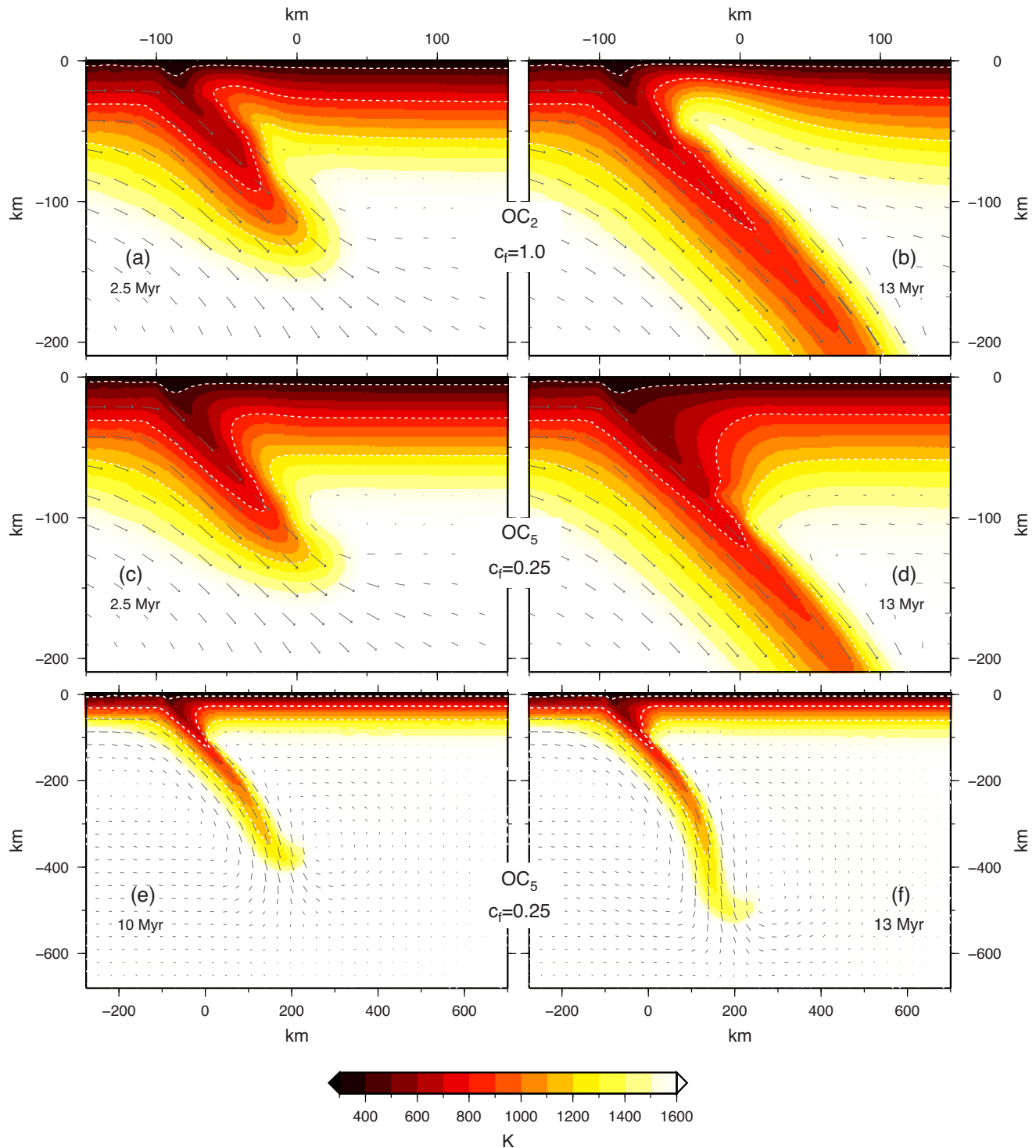
Figure 7. Thermal (colour) and velocity (black arrows) fields predicted by the OC_2 (panels a and b) and OC_5 (panels c and d) models after 2.5 (panels a and c) and 13 Myr (panels b and d) since the beginning of subduction. Panels (e) and (f) show, at the large scale, the thermal and velocity fields predicted by model OC_5 after 10 (e) and 13 Myr (f) since the beginning of subduction. The white dashed lines indicate the 400, 800 and 1200 K isotherms. OC_2: $u_s = 5$ cm yr^{-1}; $\theta_s = 45°$; $\mathbf{c_f = 1}$; OC_5: $u_s = 5$ cm yr^{-1}; $\theta_s = 45°$; $\mathbf{c_f = 0.25}$.

dragged at great depths (compare panels c and d of Fig. 10 to panels a and c of Fig. 8). The local thermal warming occurring at mantle levels in the wedge area also generates unfavorable p–T conditions for mantle hydration, which in turn limits the recirculation of light material. All these factors generate intense and localized negative and positive density anomalies, as shown in the insets of panels (c) and (d) of Fig. 10. The substitution of the scraped crust and the rising of cold mantle is responsible for shallow positive density anomalies that are considerably more intense than that predicted by the homologous 45° OC_3 model (compare panel d of Fig. 10 to panel c of Fig. 8). Conversely, at greater
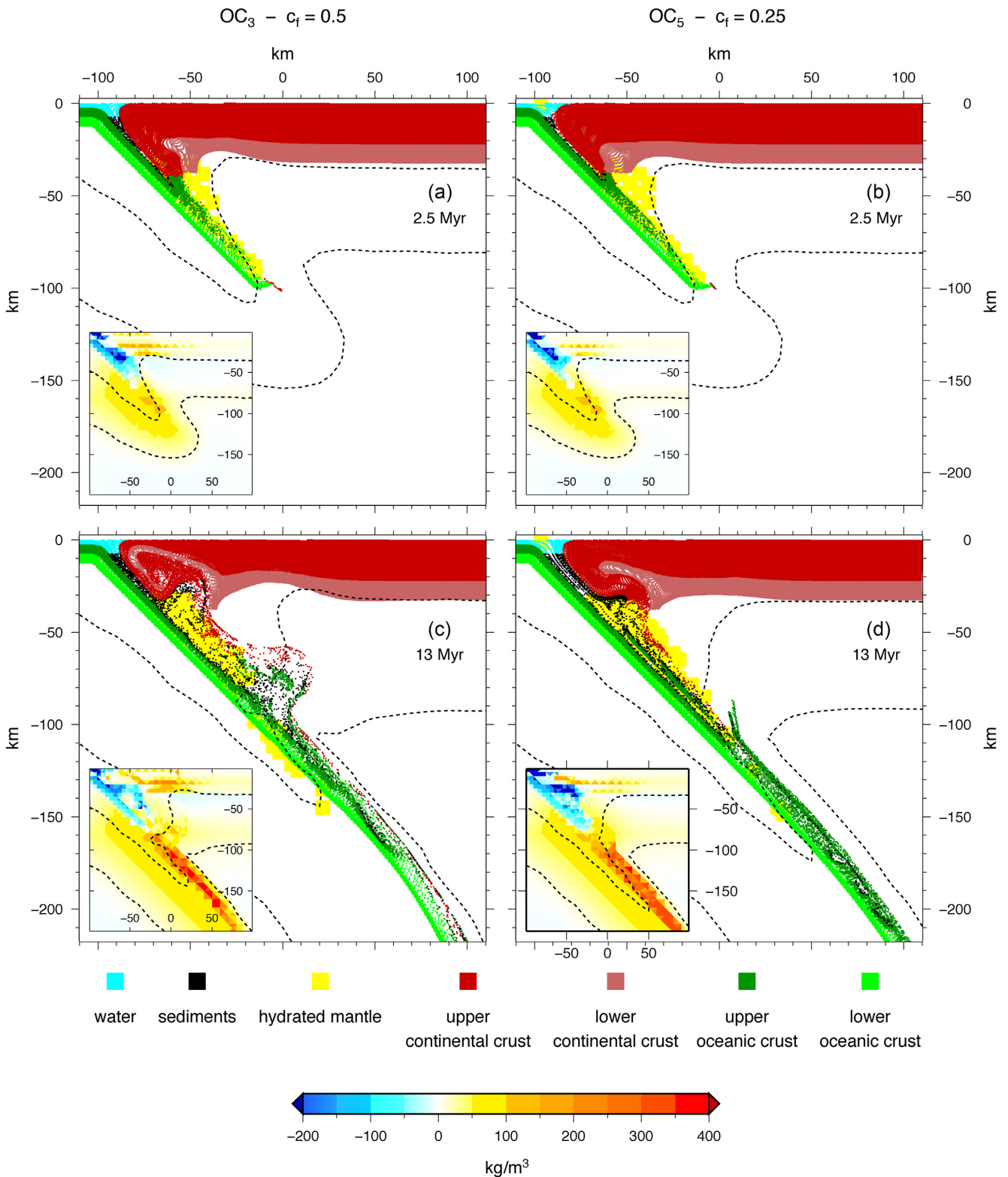
Figure 8. Marker distribution predicted by the OC_3 (panels a and c) and OC_5 (panels b and d) models after 2.5 (panels a and b) and 10 Myr (panels c and d) since the beginning of subduction. The insets in the same panels show the density anomalies at the same times. The dashed black lines indicate the 800 and 1500 K isotherms. OC_3: $u_s = 5$ cm yr^{-1}; $\theta_s = 45°$; $\mathbf{c_f = 0.5}$; OC_5: $u_s = 5$ cm yr^{-1}; $\theta_s = 45°$; $\mathbf{c_f = 0.25}$.
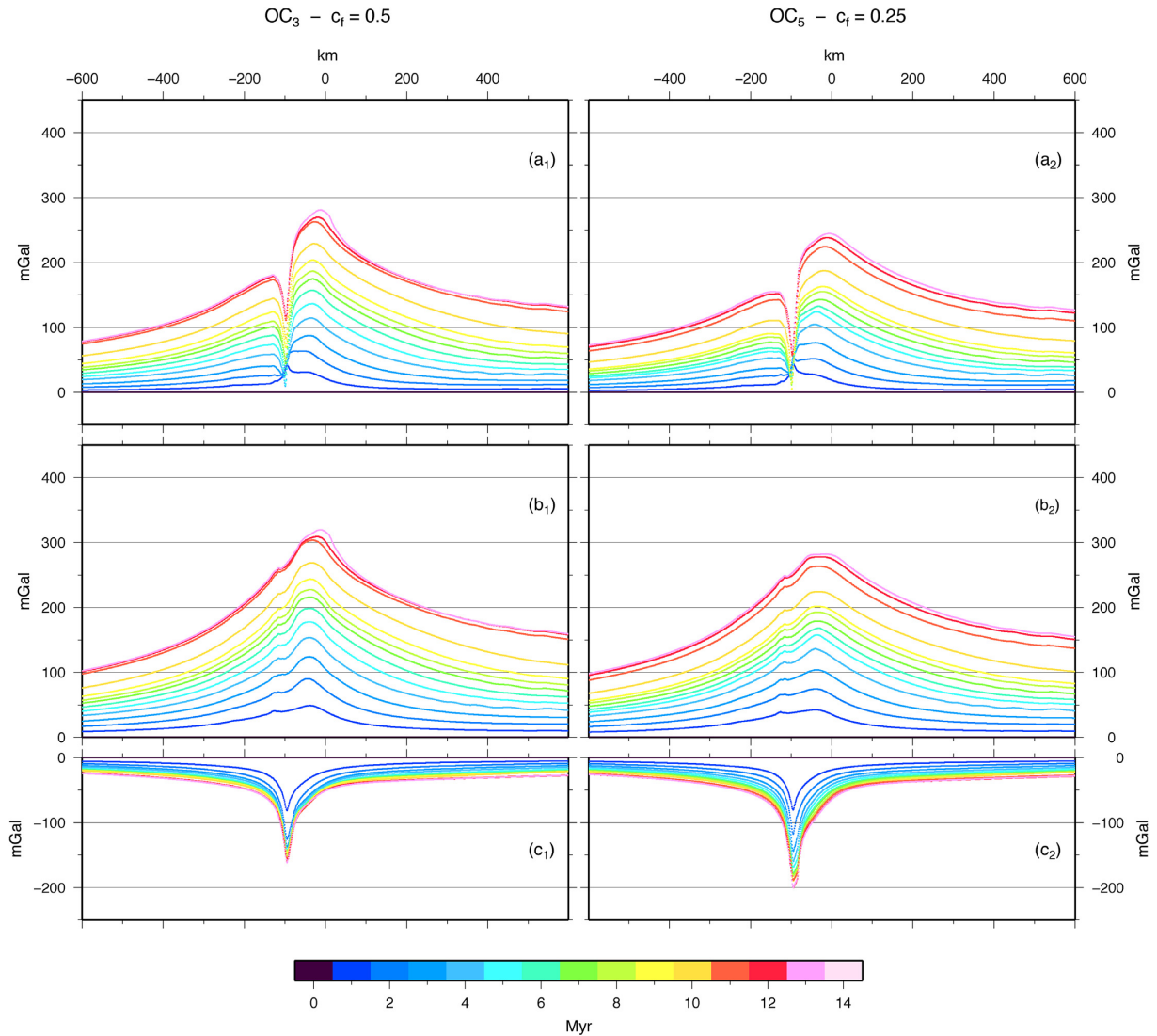
Figure 9. Gravitational contribution of the density anomalies predicted by the OC_3 (a_1) and OC_5 (a_2) models after different time intervals since the beginning of subduction. The Gravitational contribution of the sole positive density anomalies predicted by the OC_3 (b_1) and OC_5 (b_2) models. (c) Gravitational contribution of the sole negative density anomalies predicted by the OC_3 (c_1) and OC_5 (c_2) models. The profiles are plotted at 1 Myr time intervals. Colours indicate the age of subduction. OC_3: $u_s = 5$ cm yr^{-1}; $\theta_s = 45°$; **$c_f = 0.5$**; OC_5: $u_s = 5$ cm yr^{-1}; $\theta_s = 45°$; **$c_f = 0.25$**.

depths, the positive density anomalies are less intense for the 60° OC_7 model, mainly because the interior of the subducted slab remains warmer than in the 45° OC_3 model (compare panel d of Fig. 10 to panel c of Fig. 8). Regarding the negative density anomalies, the component associated with the trench trough, the subducted crust and sediments and the mantle hydration remains almost unchanged in magnitude but assumes a thinner shape along the subduction plane. Furthermore, a diffuse negative anomaly appears at the mantle level of the wedge area, similar to that predicted by the fully coupled OC_2 model (Fig. 4c). However, it is now less intense because the lower plate coupling makes the local crustal erosion due to the mantle wedging flow not accompanied by coeval and equally effective local heating (compare isotherms 800 and 1500 K in Fig. 10d, and Fig. 4c).

Fig. 11 shows the gravitational perturbation due to the density anomaly shown in Fig. 10. A decrease of approximately 20 mGal in the magnitude of the gravitational contribution due to the negative density anomalies occurs with respect to the 45° OC_3 model during the whole evolution (compare panel c of Fig. 11 to panel c_1 of Fig. 9); an increase in the gravitational contribution due to the positive density anomalies also occurs, up to more than 50 mGal in the mature stages of subduction. In addition, during evolution, the lateral extension of the gravity trough decreases with time because the absolute maximum moves towards the trench as a consequence of the intensification and localization of the shallow positive density anomaly (insets of Figs 10c and d). This behaviour is opposite of that occurring with the 45° OC_3 model. Finally, because the subducted plate reaches the olivine-spinel transition in a more vertical way, the jump in the gravitational contribution occurs earlier and more rapidly (compare Fig. 11b, to Fig. 9b_1).
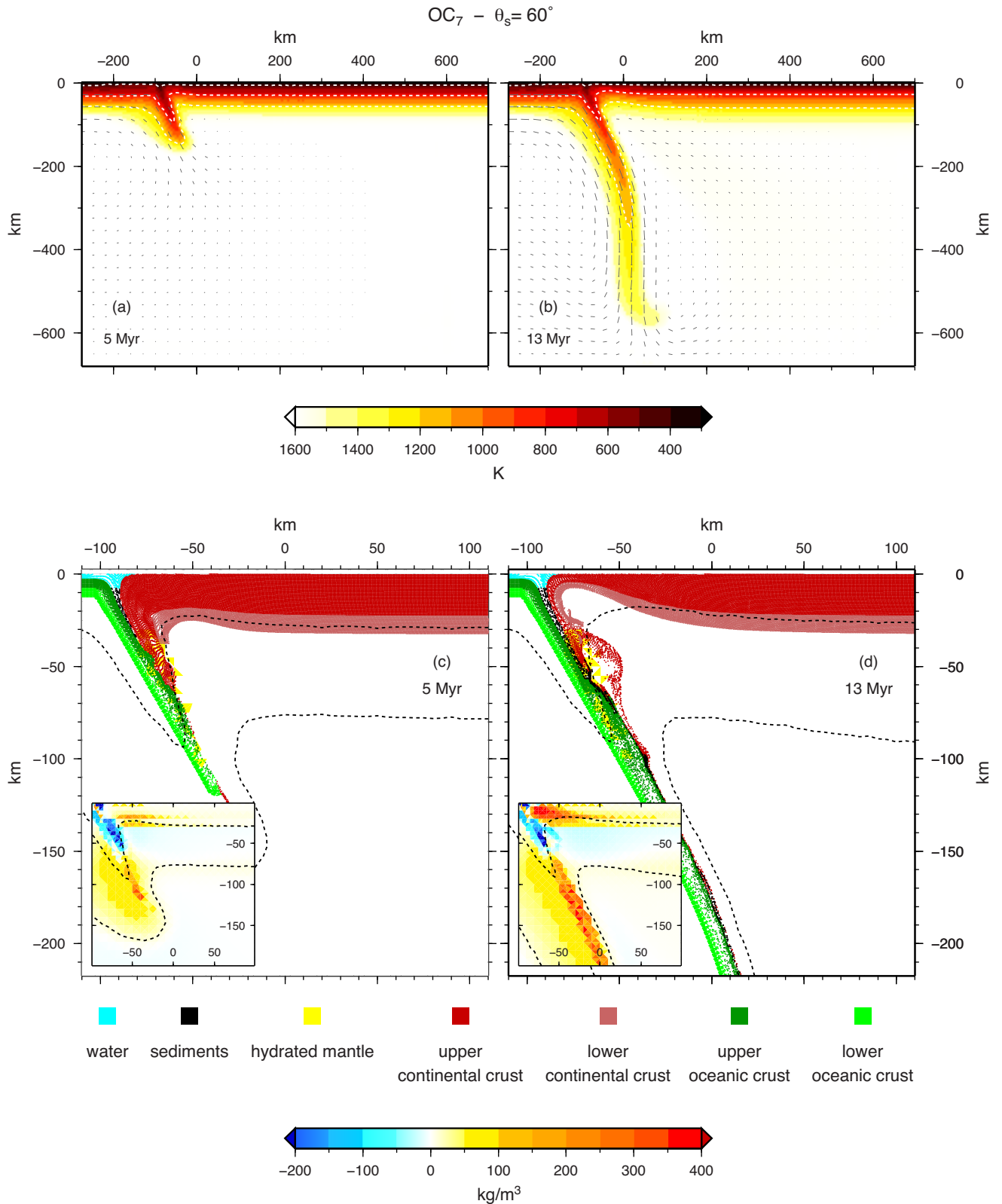
Figure 10. (a and b) Large-scale thermal (colour) and velocity field (black arrows) predicted by the OC_7 model after 5 (a) and 13 Myr (b) since the beginning of subduction. The white dashed lines indicate the 400, 800, 1200 and 1500 K isotherms. (c and d) Marker distribution predicted by the same model after 5 (c) and 13 Myr (d) since the beginning of subduction. The insets show the density anomalies at the same times. The dashed black lines indicate the 800 and 1500 K isotherms. OC_7: $u_s = 5$ cm yr^{-1}; $\boldsymbol{\theta_s = 60°}$; $c_f = 0.5$.
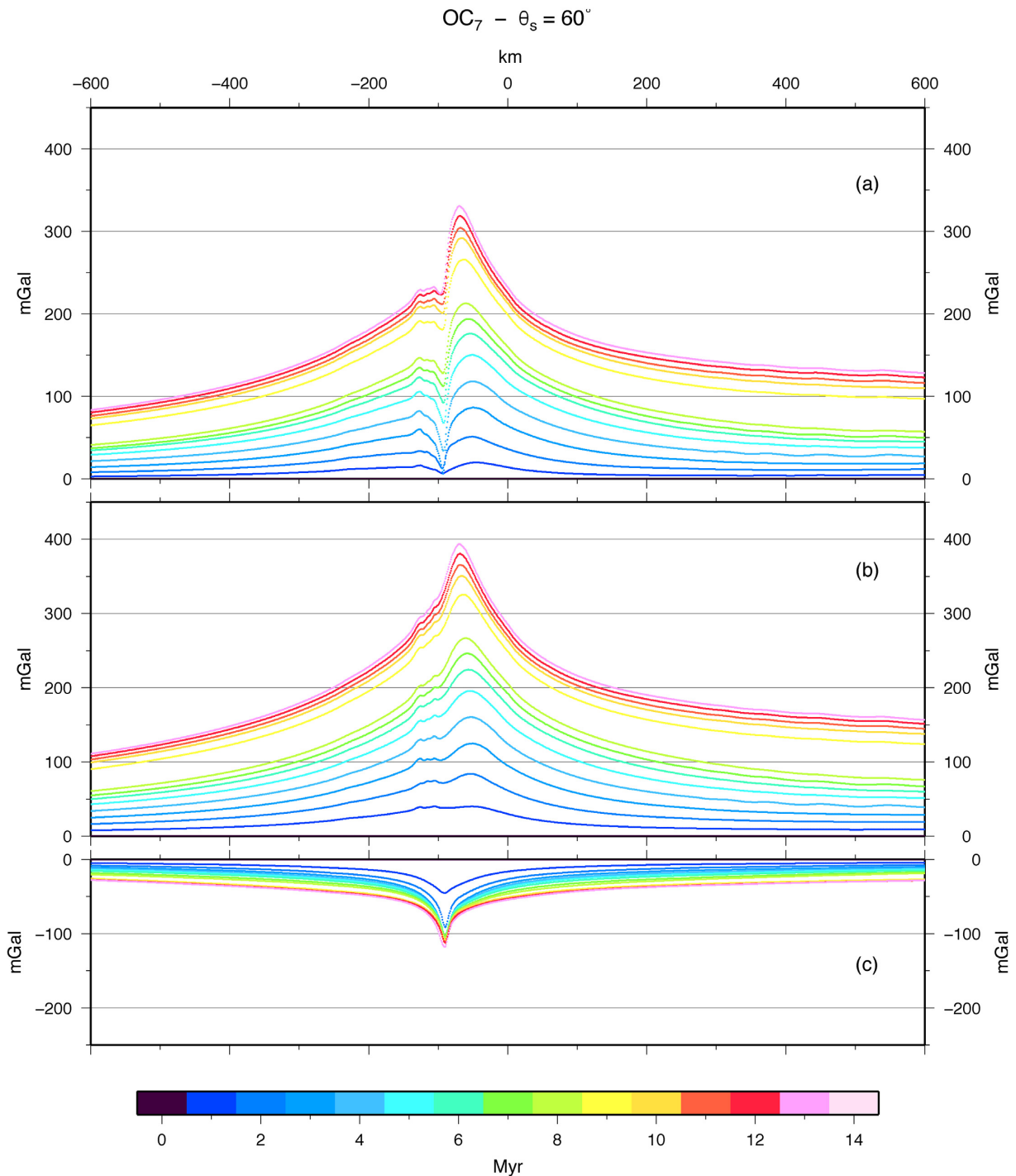
Figure 11. (a) Gravitational contribution of the density anomalies predicted by the OC_7 model after different time intervals since the beginning of subduction. (b) Gravitational contribution of the sole positive density anomalies. (c) Gravitational contribution of the sole negative density anomalies. The profiles are plotted at 1 Myr time intervals. Colours indicate the age of subduction. OC_7: $u_s = 5 \, \text{cm yr}^{-1}$; $\boldsymbol{\theta_s = 60°}$; $c_f = 0.5$.

3.2.3 Subduction velocity u_s

To identify the effects induced by a different subduction velocity on the gravitational field, we compare the predictions from three models characterized by the average values of all the characteristic parameters, with the exception of the assumed subduction velocity, set equal to $8 \, \text{cm yr}^{-1}$ (OC_6 model), $5 \, \text{cm yr}^{-1}$ (OC_3 model) and $2 \, \text{cm yr}^{-1}$ (OC_{14} model) (panels a_i, b_i and c_i of Fig. 12, respectively). In this case, the comparison is not performed after the same time span since the beginning of the subduction but rather after a different time span for each model, when the same amount of ocean is consumed, specifically 200 and 600 km, corresponding to approximately 2.5 and 7.5 Myr for $u_s = 8 \, \text{cm yr}^{-1}$, 4 and 12 Myr for $u_s = 5 \, \text{cm yr}^{-1}$, and 10 and 32 Myr for $u_s = 2 \, \text{cm yr}^{-1}$. The depth of 200 km is chosen because the subducted
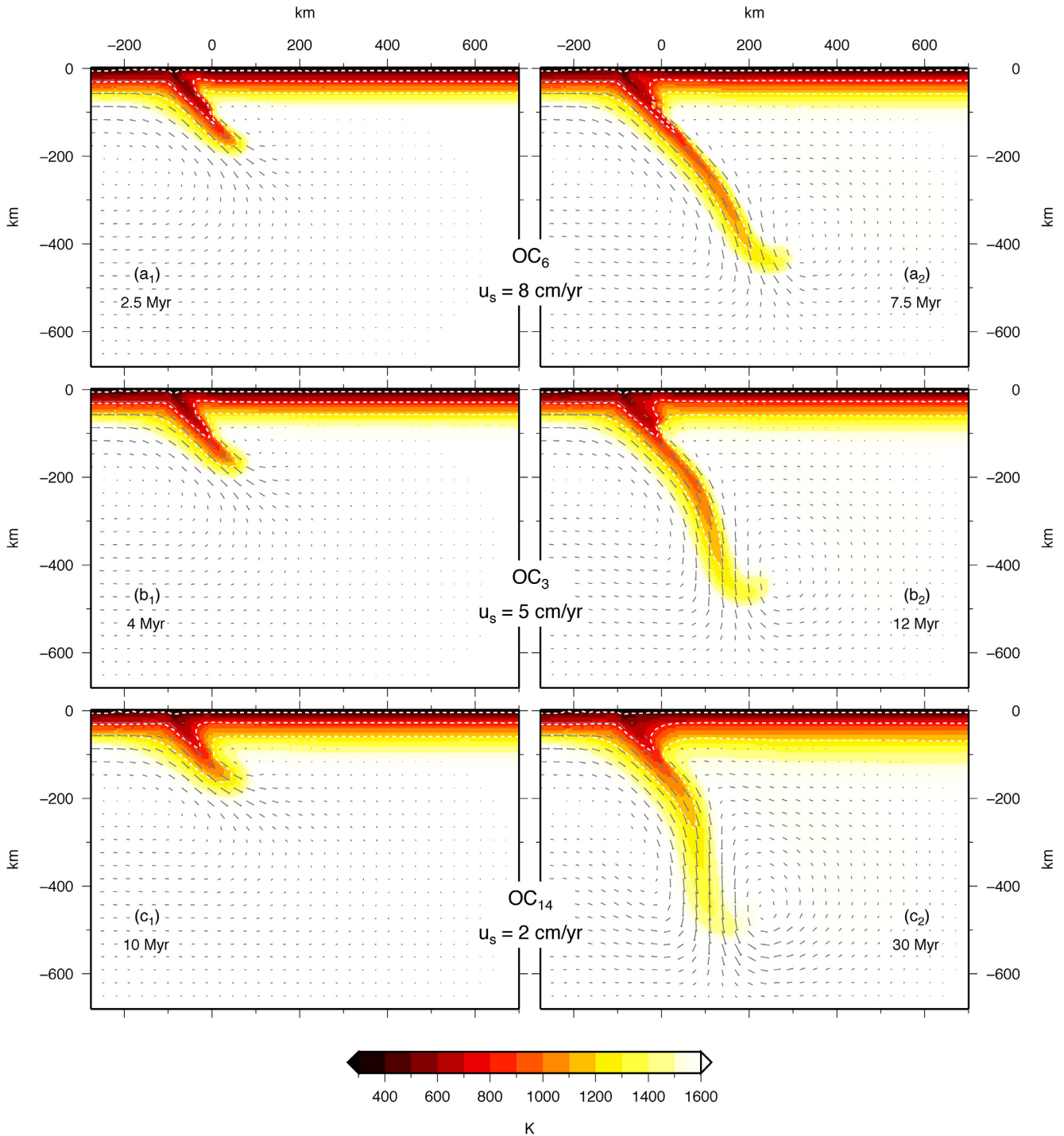
Figure 12. Large-scale thermal (colour) and velocity (black arrows) fields predicted by OC_6 (panels a_1 and a_2), OC_3 (panels b_1 and b_2) and OC_{14} (panels c_1 and c_2) when the same extent of ocean is consumed, specifically 200 km (2.5 Myr for the OC_6 model, panel a_1, 4 Myr for the OC_3 model, panel b_1 and 10 Myr for the OC_{14} model, panel c_1) and 600 km (7.5 Myr for the OC_6 model, panel a_2, 12 Myr for OC_3 model, panel b_2 and 30 Myr for the OC_{14} model, panel c_2). The white dashed lines indicate the 400, 800 and 1200 K isotherms. OC_3: $\mathbf{u_s = 5\ cm\ yr^{-1}r}$; $\theta_s = 45°$; $c_f = 0.5$; OC_6: $\mathbf{u_s = 8\ cm\ yr^{-1}}$; $\theta_s = 45°$; $c_f = 0.5$; OC_{14}: $\mathbf{u_s = 2\ cm\ yr^{-1}}$; $\theta_s = 45°$; $c_f = 0.5$.

slab is well developed but still unaffected by the olivine-spinel phase boundary, while the depth of 600 km is chosen because it is comparable with the maximum length of the Benioff planes.

The major effects of a change in subduction velocity are in the thermal field of the wedge area and of the subducted slab (Fig. 12). From the general thermomechanical perspective, the more efficient advection characterizing the high-velocity model OC_6 of panels a_1 and a_2 is responsible for a thinner and colder slab that favours maintaining the prescribed subduction dip angle at great depths (panel a_2 of Fig. 12, compared to b_2 and c_2). In addition, the thermal field remains almost unchanged far from the trench (Fig. 12). A decrease in the subduction

velocity results in a thermal thickening of the subducted slab at shallow depths, in a more effective thermal erosion at high depths, in a significant variation of the deep dip and in a thermal thickening of the upper plate (Fig. 12, panels b_1, b_2, c_1 and c_2).

If we focus on the wedge area and on the distribution of the material particles (Fig. 13, with the fast OC_6 model in panels a and c and the slow OC_{14} model in panels b and d), it is evident that the thermal differences are not accompanied by equally significant differences in the distribution of material particles and by significant differences in the shallow density anomalies (compare panels c and d of Fig. 13 to panel c of Fig. 8).

Instead, at the deep lithosphere mantle level and at great depths, the thermal thickening characterizing the slowest subduction velocity model OC_{14} induces a widespread positive density anomaly close to the lithosphere base and a positive anomaly associated with the subducted slab with a thickness of almost one and a half times (compare panels e and f of Fig. 13).

Fig. 14 shows the gravitational perturbation at times when the subducted slabs reach depths of 200 km (panels a_1, b_1 and c_1) and 600 km (panels a_2, b_2 and c_2) from the fastest to the slowest models, from top to bottom. Although the contribution of the negative density anomalies (dotted black lines) is not significantly influenced by the subduction velocity, the contribution from the positive density anomalies (dashed black lines) increases as the subduction velocity decreases due to the thermal thickening of the subducted plate and to the anomaly of the positive density that develops near the base of the lithosphere (also see the insets of panels e and f of Fig. 13). The latter, due to its widespread nature, also intensifies the asymmetry in the gravity profile, increasing the difference between the minimum value of the gravitational contribution and its far field value as the subduction velocity decreases. Finally, note that at any time, the width of the gravity trough increases as the subduction velocity decreases.

It is certainly interesting to compare the rate of change of the gravity anomalies for different subduction velocities. Based on the considerations made in the previous paragraphs regarding the variations in time of the areal distribution and of the magnitude of the density anomalies obtained for different subduction velocities, we expect that the rate of change of the gravity anomalies varies significantly as the subduction velocity varies. This is in fact what occurs in Fig. 15, where the rates of change for the OC_6 ($u_s = 8$ cm yr^{-1}) and OC_{14} ($u_s = 2$ cm yr^{-1}) models are presented. As expected, the differences can be significant and the rate of change decreases to one third when the subduction velocity decreases from 8 to 2 cm yr^{-1} (Fig. 15), making slow subduction appear to be a quasi-static process even from the gravitational perspective. However, note that when the rates of change are normalised with respect to the corresponding subduction velocity, the graphs, with the exception of some differences due to local-scale features, become comparable (Fig. 16), making it possible to estimate a maximum rate of change equal to 0.008 μGal yr^{-1} for each cm/yr of subduction velocity.

3.2.4 Ocean–ocean context

Here, we illustrate only the major differences between predictions from ocean–ocean models and the corresponding ocean–continent models. Fig. 17 shows the marker distribution and the density anomalies (in the insets) predicted by the OO_1, OO_4 and OO_7 models, with the coupling factor decreasing from top to bottom, from 1, 0.5 and 0.25, after 2.5 and 13 Myr from the beginning of subduction, at a velocity of 5 cm yr^{-1}, with a subduction dip angle of 45°. With respect to the corresponding ocean–continent-type models (models OC_2 - Fig. 4, OC_3 and OC_5 - Fig. 8), a generally larger amount of light material (both crust and sediments) recirculates in the wedge where a wider hydrated area is further developed. A significant erosion of the crust belonging to the upper plate occurs, allowing the exhumation of the recirculated light material. This peculiar mass redistribution is at the origin of the very intense and shallow negative density anomalies that develop over an area wider than 60 km.

Fig. 18 shows the gravitational contribution at 4 and 12 Myr from the initiation of subduction for the same models shown in Fig. 17, with the coupling factor decreasing from top to bottom, from 1, 0.5 and 0.25. Unlike the ocean–continent context, plate decoupling does not significantly affect the shape of the gravitational contribution pattern. The aspects that deserve to be noticed are a slight increase in the positive contribution accompanying the decrease in the coupling of the plates and a slightly more significant increase in the negative contribution with the increase in the coupling (compare panels a and c of Fig. 18). The most important characteristic is instead the greater width of the gravity trough, on the order of more than 200 km, that occurs in the ocean–ocean environments compared to 100 km in the ocean–continental environment (Fig. 14, panel b_2) due to the peculiar wider distribution of the recycled material (Fig. 17).

4 CASE STUDIES: THE SUMATRA AND MARIANA COMPLEXES

4.1 Tectonic setting

The Sumatran and Mariana subductions are considered to be two classical tectonic settings representative of an ocean–continent subduction and an ocean–ocean subduction.

The Indonesian Island of Sumatra represents an interesting natural laboratory for geodynamic and geophysical investigations because it is one of the most active regions in the world. In fact, numerous large earthquakes have occurred in the Sumatra subduction zone within the last two centuries, including the magnitude 9.3 Sumatra-Andaman earthquake on 26 December 2004 (Gamage 2017). The subduction zone of Sumatra results from the underthrusting of the Indo-Australian Plate subducting beneath the Sunda plate, Andaman and Burma microplate (Shapiro *et al.* 2008; Gamage 2017) along three main trenches, Java, Sunda and Andaman–Nicobar (Nielsen *et al.* 2004), with a convergence
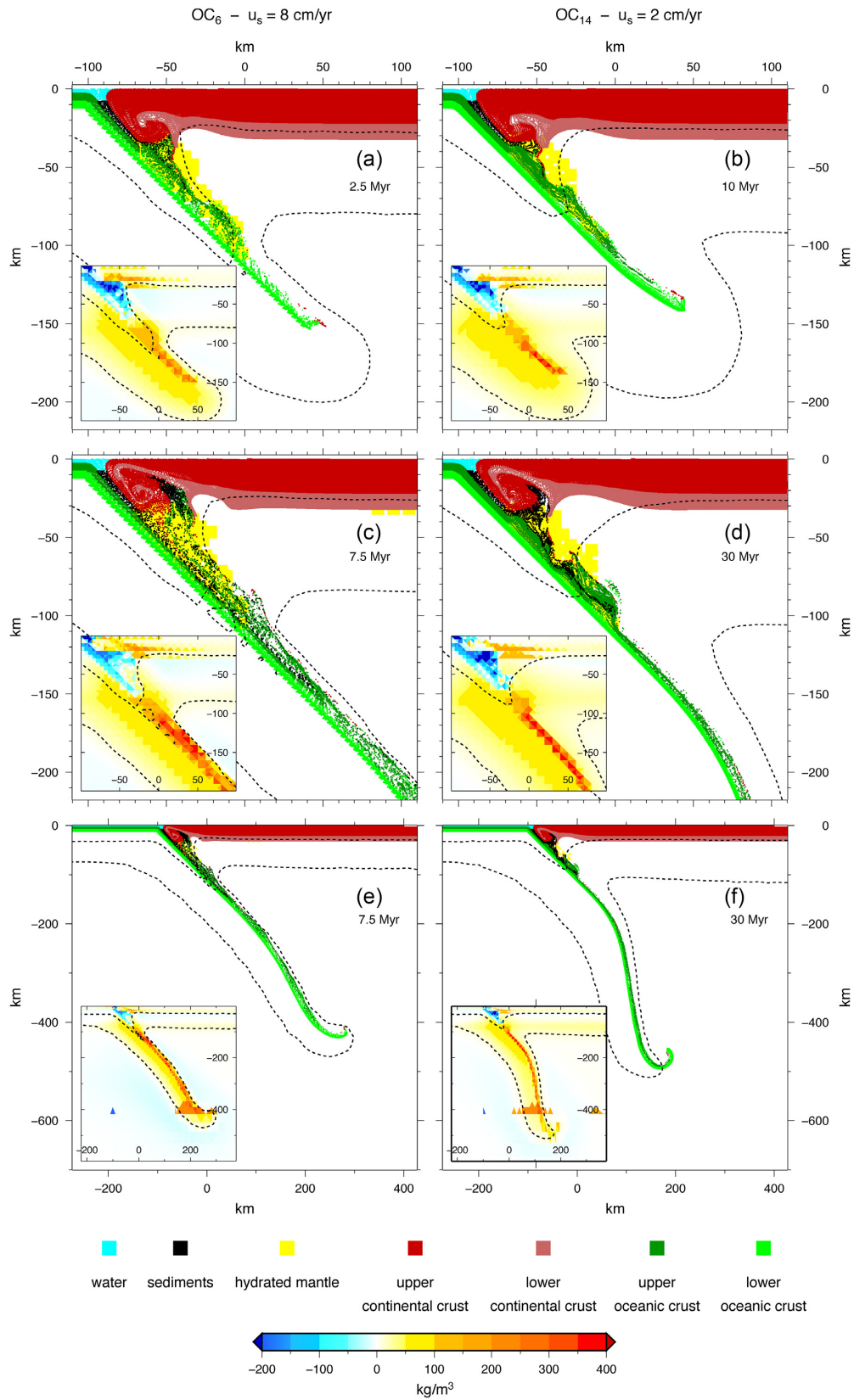
Figure 13. Marker distributions predicted by OC_6 (panels a and c) and OC_14 (panels b and d) when the same extent of ocean is consumed, specifically 200 km (2.5 Myr for the OC_6 model, panel a, and 10 Myr for the OC_{14} model, panel b) and 600 km (7.5 Myr for the OC_6 model, panel c, and 30 Ma for OC_{14} model, panel d). Panels e and f show the large-scale marker distributions predicted by OC_6 after 7.5 Myr (e) and OC_{14} after 30 Myr (f) since the beginning of subduction. The insets in all panels show the density anomalies at the same times. The dashed black lines indicate the 800 and 1500 K isotherms. OC_6: $\mathbf{u}_s = \mathbf{8}$ **cm yr**$^{-1}$; $\theta_s = 45°$; $c_f = 0.5$; OC_{14}: $\mathbf{u_s} = \mathbf{2}$ **cm yr**$^{-1}$; $\theta_s = 45°$; $c_f = 0.5$.
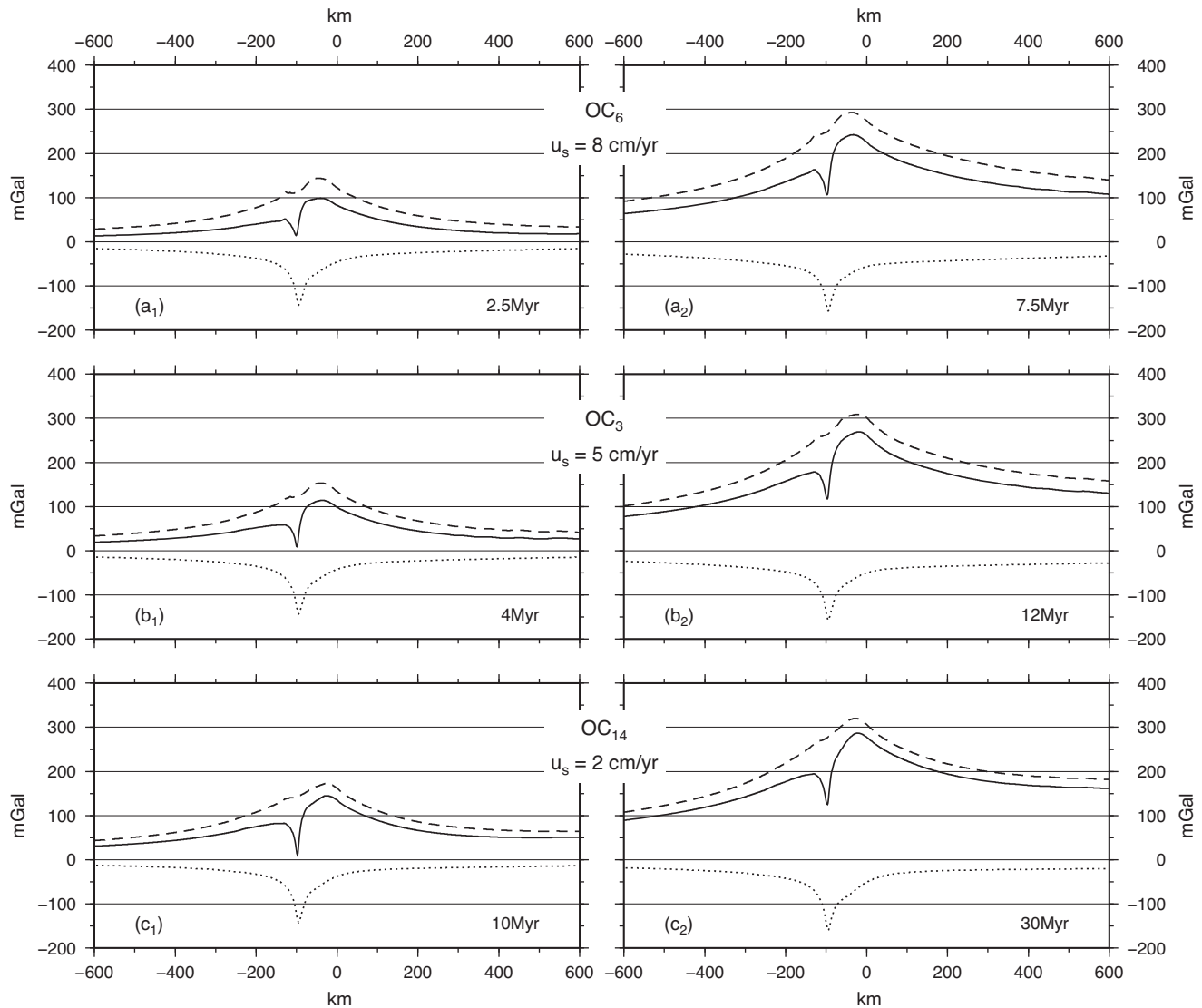
Figure 14. Solid lines indicate the gravitational contribution of the density anomalies predicted by OC_6 (panels a_1 and a_2), OC_3 (panels b_1 and b_2) and OC_{14} (panels c_1 and c_2) when 200 km (panels a_1, b_1 and c_1) and 600 km (panels $a_{1qw2\grave{e}+\grave{o}\grave{a}w-----2}$, b_2 and c_2) of ocean is consumed. Dashed and dotted lines indicate the gravitational contribution of the sole positive and negative density anomalies, respectively, for the same models in the same configuration. OC_3: $\mathbf{u_s = 5\ cm\ yr^{-1}}$; $\theta_s = 45°$; $c_f = 0.5$; OC_6: $\mathbf{u_s = 8\ cm\ yr^{-1}}$; $\theta_s = 45°$; $c_f = 0.5$; OC_{14}: $\mathbf{u_s = 2\ cm\ yr^{-1}}$; $\theta_s = 45°$; $c_f = 0.5$.

velocity that decreases northward, from 7.23 cm yr^{-1} off Java to 4.3 cm yr^{-1} in Andaman and approximately 5.5 cm yr^{-1} in the northern Sumatra (Moeremans *et al.* 2014). The Andaman-Sumatra section of subduction represents an example of oblique subduction resulting in slip partitioning into a trench-normal component at the plate interface (Moeremans *et al.* 2014) and a strike-slip component along the Great Sumatra Fault (GSF, Moeremans *et al.* 2014; Bradley *et al.* 2017) and possibly the West Andaman Fault (WAF, Moeremans *et al.* 2014). The convergence is nearly orthogonal along the Java trench and subparallel along the Andaman Islands trench (Moeremans *et al.* 2014). The transition between the two subduction regimes occurs south of the Sunda Strait (Malod & Kemal 1996). Here, where the plate boundary geometry changes abruptly, tomography and seismic studies show slab tearing, with a distinct gap in seismicity between depths of 300 and 500 km beneath the central Sunda (Java) block (Kundu & Gahalaut 2011). In addition to strong strain partitioning, the area presents other peculiar tectonic settings, such as active spreading in the backarc beneath the Andaman Sea and lateral age variability of the incoming Indian Plate. Beneath Sumatra, a young oceanic lithosphere of approximately 40–60 Myr is subducting (Schluter *et al.* 2002; Shapiro *et al.* 2008), corresponding to a thickness of 80–100 km (Turcotte & Schubert 2002). In contrast, off Java and Andaman Islands, the age of the oceanic lithosphere varies from 70 to 120 Myr and from 70 to 90 Myr (Moeremans *et al.* 2014). This aspect influences the style of deformation and seismicity along the entire arc. Where the lithosphere is younger and consequently warmer and more buoyant, the subducting plate and the mantle wedge appear to be strongly coupled with a Wadati-Benioff zone of approximately 30–45° (Shapiro *et al.* 2008; Kundu & Gahalaut 2011). In contrast, in adjacent areas to the north and south, the seismic zones have higher dip angles (Shapiro *et al.* 2008; Kundu & Gahalaut 2011).
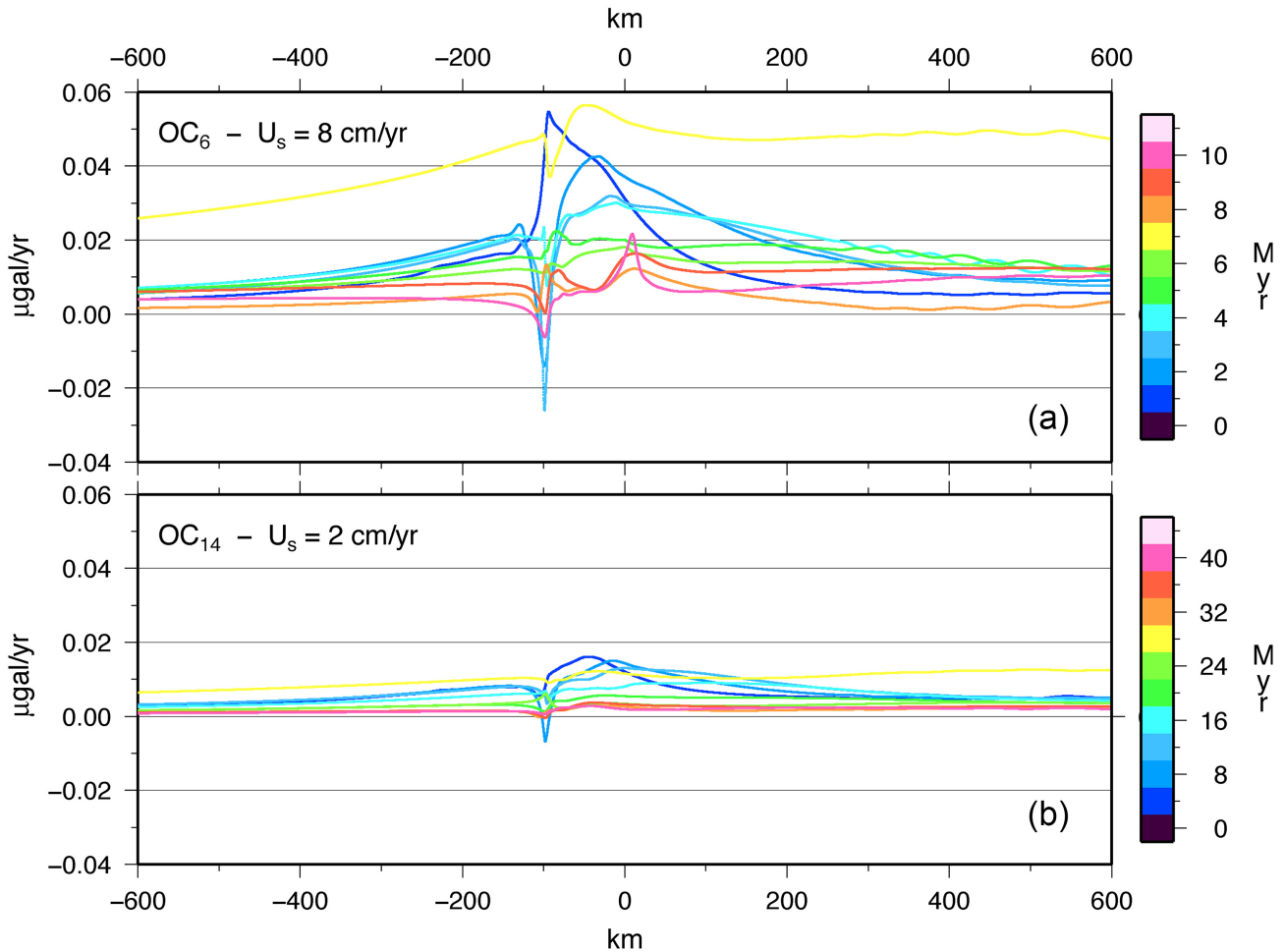
Figure 15. Rate of change of the gravitational contribution of the density anomalies predicted by OC_6 (panel a) and OC_{14} (panel b) after different time intervals since the beginning of subduction. The profiles are plotted at 1 and 4 Myr time intervals for OC_6 (panel a) and OC_{14} (panel b). OC_6: **u_s=8 cm yr^{-1}**; θ_s=45°; c_f =0.5; OC_{14}: **u_s=2 cm yr^{-1}**; θ_s=45°; c_f =0.5.

The variability in the convergence velocity, particularly in the component perpendicular to the trench, as well as in the dip angles, from 30° to −45° to higher angles, indicates that the appropriate velocity values of 8, 5 and 2 cm yr^{-1} (with 5 cm yr^{-1} as the most representative value) and the three dip angles of 30°, 45° and 60° (with 45° the most representative one) are appropriate for the modelling of the EIGEN-6C4 gravitational disturbance characterized by a 2-D dipolar pattern perpendicular to the trench, first requiring a 2-D modelling approach as performed herein to capture the characteristics of the gravity pattern.

Regarding the age of subduction, for these case studies, we take as a reference the youngest age of the Sumatran oceanic lithosphere of 40 Myr.

Taken collectively, within the frame of a 2-D approach used to model the 2-D pattern of the EIGEN-6C4 gravitational disturbance, similar features can be found in the Izu-Bonin-Mariana (IBM) trench. Stretching for 2800 km (Pearce *et al.* 2015) accommodates the oblique west-dipping subduction (Faccenda *et al.* 2018; Kong *et al.* 2018) of the Pacific beneath the Philippine Sea Plate at a velocity of approximately 9 cm yr^{-1} along the Izu–Bonin arc and 5 cm yr^{-1} along the Mariana arc (Kong *et al.* 2018). Since the Eocene, the plate-tectonic history of this region has been affected both by multiple clockwise rotation events of the Philippine Sea Plate, as evidenced by paleomagnetic data (Hall *et al.* 1995; Sdrolias *et al.* 2004), and by the northeast migration of the triple junction between the Eurasian, Philippine Sea, and Pacific Plates from 30 to 17 Myr (Castle & Creager 1999). Along with the triple junction motion, the northern Izu-Bonin trench retreated over 1000 km to the northeast, producing the opening of the Shikoku basin (between 25 and 15 Myr, Hall *et al.* 1995; Anderson *et al.* 2017), while the Mariana trench retreated 400 km to the northeast (Castle & Creager 1999; Anderson *et al.* 2017) accompanied by the opening of the Parece Vela basin (Anderson *et al.* 2017). The age of the subducting lithosphere varies along the arc system from approximately 135 Myr at the northern Izu-Bonin trench to over 150 Myr at the Mariana trench (van der Hilst & Seno 1993), corresponding to a thickness of 160 km (Turcotte and Schubert, 2002). Several studies of seismic tomography and seismicity have clearly defined the geometry of the subducting slab in depth. The variation in the geometry of the subducted slab along the arc is a peculiar aspect of the region. van der Hilst & Seno (1993) proposed that beneath the Izu-Bonin arc, the combination of young oceanic lithosphere and rapid trench migration produced a shallow subduction angle, with the slab deflecting horizontally at the 670 km discontinuity (van der Hilst & Seno 1993; Miller *et al.* 2005; Anderson *et al.* 2017; Kong
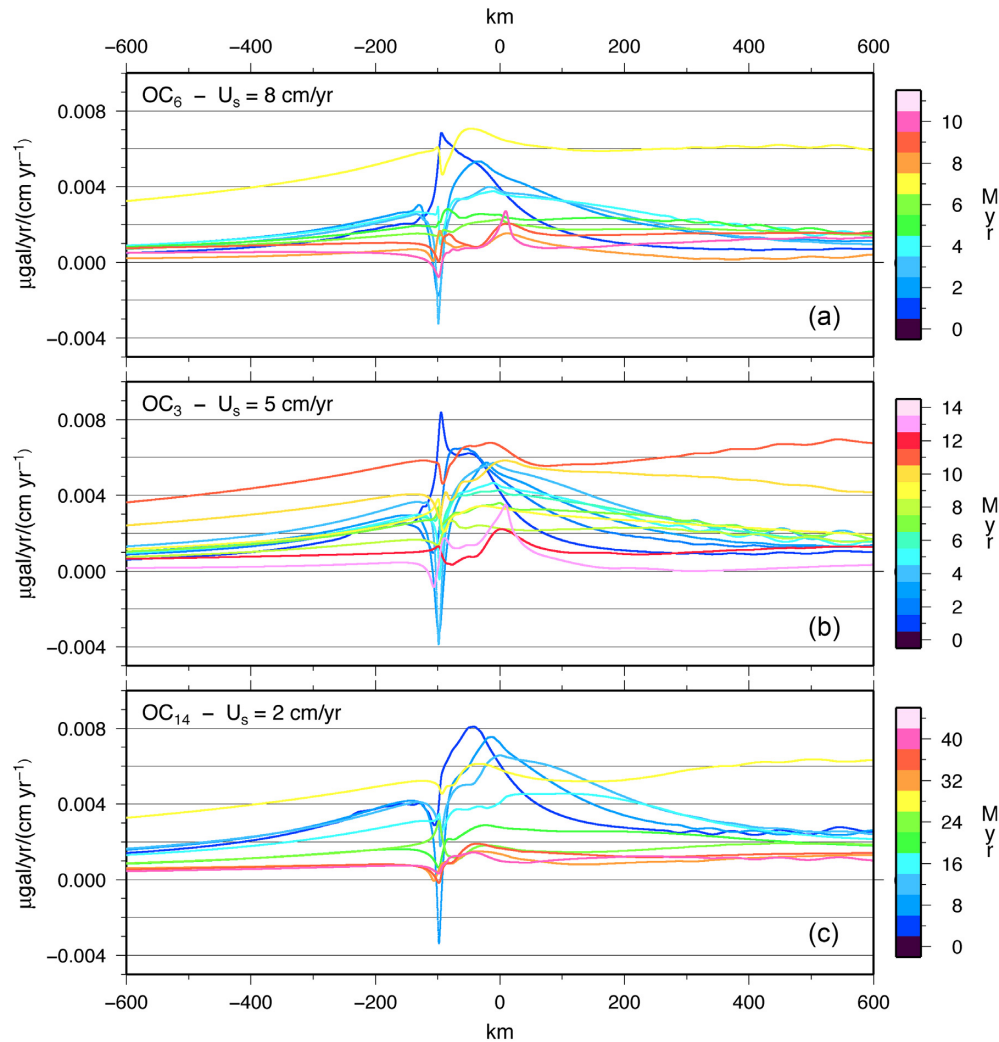
Figure 16. Rate of change, normalized with respect to the corresponding prescribed subduction velocity, of the gravitational contribution of the density anomalies predicted by OC_6 (panel a), OC_3 (panel b) and OC_{14} (panel c), after different time intervals since the beginning of subduction. The profiles are plotted at 1 Myr for OC_6 (panel a) and OC_3 (panel b) and at 4 Myr time interval for OC_{14} (panel c). OC_3: $\mathbf{u_s = 5\ cm\ yr^{-1}}$; $\theta_s = 45°$; $c_f = 0.5$; OC_6: $\mathbf{u_s = 8\ cm\ yr^{-1}}$; $\theta_s = 45°$; $c_f = 0.5$; OC_{14}: $\mathbf{u_s = 2\ cm\ yr^{-1}}$; $\theta_s = 45°$; $c_f = 0.5$.

et al. 2018). In contrast, southward, below the Mariana trench, the slab plunges steeply into the lower mantle (Faccenda *et al.* 2018; Holt *et al.* 2018). The abrupt change from a horizontal to a vertical slab is accommodated by tearing at the junction of the Izu-Bonin and Mariana arcs at ∼26°N, where the Ogasawara Plateau occurs at the junction (Anderson *et al.* 2017). In fact, tomographic and seismic images reveal a distinct change in the seismic property of the subducted Pacific plate beneath the Izu-Bonin arc, with a seismic gap at approximately 300–400 km, interpreted as a probable slab tear (Kong *et al.* 2018). A N–S trending slab tear is also suggested at the southern end of the Mariana arc, known as the Challenger Deep (Miller *et al.* 2006).

Due to the similarities in convergence velocity, dip angles and age, as well as their variability along the trench, we consider the Sumatra values for these parameters to also be appropriate for the Mariana case study, focusing on the effects of the most important difference between these two types of subduction, namely, the nature of the overriding plate, oceanic versus continental.

4.2 Regional gravity pattern

Fig. 19 shows a regional map of the gravity disturbance in the surroundings of the Sumatra and Mariana subduction complexes based on the static global combined gravity field model EIGEN-6C4 (Förste *et al.* 2014) and evaluated in the spherical approximation at a height $h_S = 5$ km above the spheroid of radius $R = 6378.137$ km. We consider this altitude to smooth slightly the geodetic signal and make it more suitable to be compared with the modelled one. The geodetic functional gravity disturbance is defined as the difference between the magnitude of the gravity g and the magnitude of the normal gravity γ:

$$\delta g\,(h, \lambda, \phi) = g\,(h, \lambda, \phi) - \gamma\,(h, \phi),\qquad(8)$$
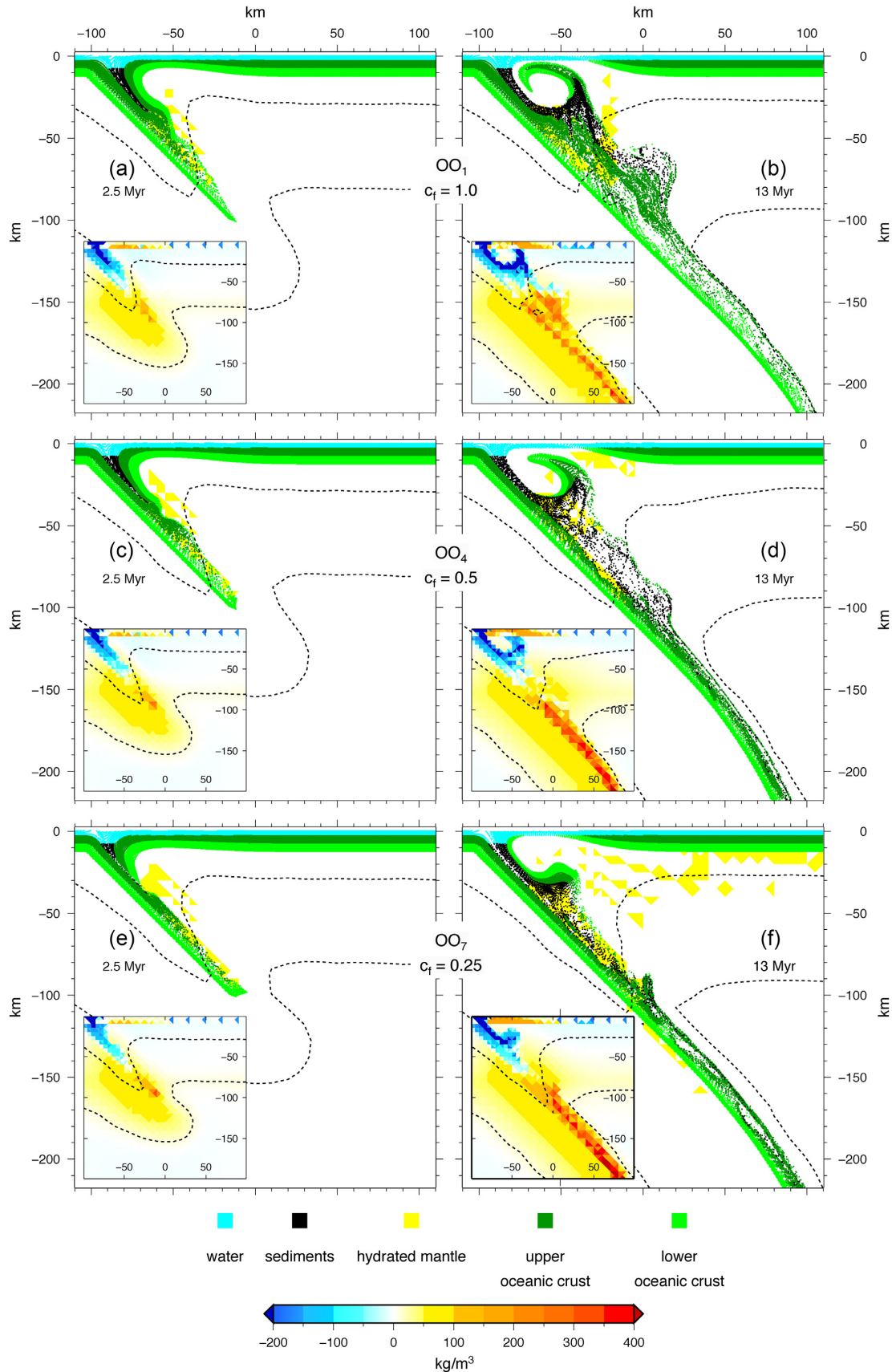
Figure 17. Marker distribution predicted by OO_1 (panels a and b), OO_4 (panels c and d) and OO_7 (panels e and f) after 2.5 (panels a, c and e) and 13 Myr (panels b, d and f) since the beginning of subduction. The insets in the same panels show the density anomalies at the same times. The dashed black lines indicate the 800 and 1500 K isotherms. OO_1: $u_s = 5$ cm yr^{-1}; $\theta_s = 45°$; $\mathbf{c_f = 1}$; OO_4: $u_s = 8$ cm yr^{-1}; $\theta_s = 45°$; $\mathbf{c_f = 0.5}$; OO_7: $u_s = 2$ cm yr^{-1}; $\theta_s = 45°$; $\mathbf{c_f = 0.25}$.
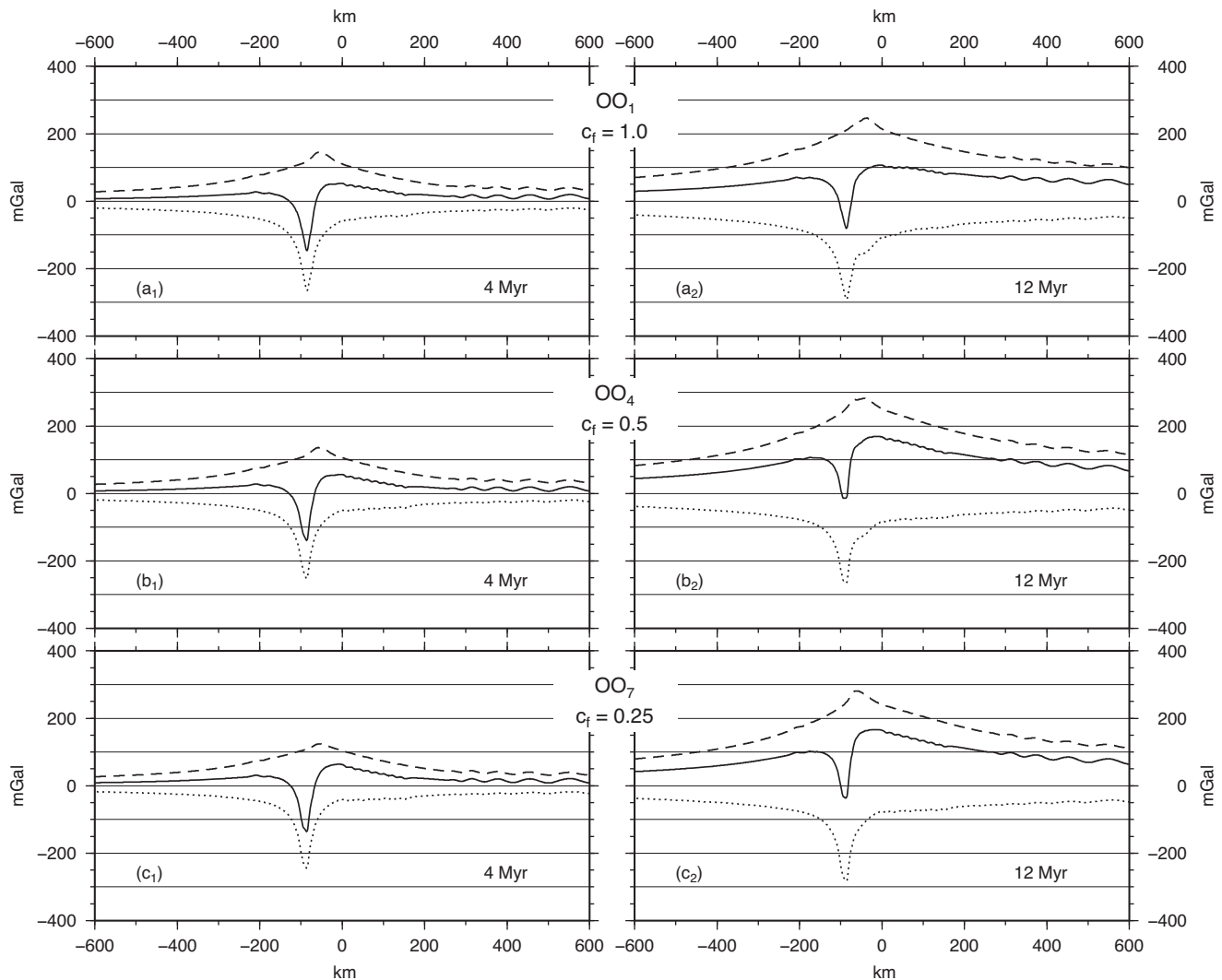
Figure 18. Solid lines indicate the gravitational contribution of the density anomalies predicted by OO_1 (panels a_1 and a_2), OO_4 (panels b_1 and b_2) and OO_7 (panels c_1 and c_2) after 4 (panels a_1, b_1 and c_1) and 12 Myr (panels a_2, b_2 and c_2) since the beginning of subduction. Dashed and dotted lines indicate the gravitational contribution of the sole positive and negative density anomalies, respectively, for the same models in the same configuration. OO_1: $u_s = 5$ cm yr^{-1}; $\theta_s = 45°$; $\mathbf{c_f=1}$; OO_4: $u_s = 8$ cm yr^{-1}; $\theta_s = 45°$; $\mathbf{c_f=0.5}$; OO_7: $u_s = 2$ cm yr^{-1}; $\theta_s = 45°$; $\mathbf{c_f=0.25}$.

where λ is the ellipsoidal longitude, ϕ is the ellipsoidal latitude and h is its height above the sea level. Among others, this functional is the most suitable for a direct comparison with our model predictions, because both normal gravity and actual gravity are calculated in the same point, without introducing any other reference point.

Fig. 19 includes for each subduction complex three profiles perpendicular to the trench, along which the observed gravity disturbance will be compared to the modelled gravity disturbance. These profiles are chosen in order to sample three different regions of the subduction complex, taken collectively as representatives of the whole arc, being each of them perpendicular to a different sector of the arc itself.

The two settings portray similar gravity features away from the trench region over the upper plate, characterized by a widespread positive gravity disturbance up to 200 mGal in both the continental and oceanic domains. Differences are instead visible over the lower plates, with gravity disturbances very low, close to zero, over the oceanic plate at Sumatra and higher gravity positive values characterizing the upper oceanic plate of the Mariana subduction. In the proximity of the trench, the map shows the bipolar trend typical of the subduction complexes, and beyond the variability depending on the position along each arc, there are some features that are peculiar of each subduction context: ocean–ocean and ocean–continent. For the ocean–continent subduction, the peak-to-peak gravity disturbance varies from approximately 240 mGal in the southern part to 280 mGal in the central portion and to 140 mGal to the north. For the ocean–ocean subduction, the peak-to-peak gravity disturbance is generally higher, approximately 30 per cent, varying from 310 mGal in the south, 270 mGal in the centre and 200 mGal to the north. In addition, for ocean–ocean subduction, the gravity disturbance across the trench is characterized by a well-developed single minimum as low as -220 mGal, and for the ocean–continent subduction, a single minimum is not well defined, and a negative value that is approximately a factor two smaller, at most -120 mGal, is observed. Finally, the lateral extent of the gravitational contribution trough is smaller across the Sumatra (smaller than 200 km) than across the Mariana (larger than 300 km) subduction complex.
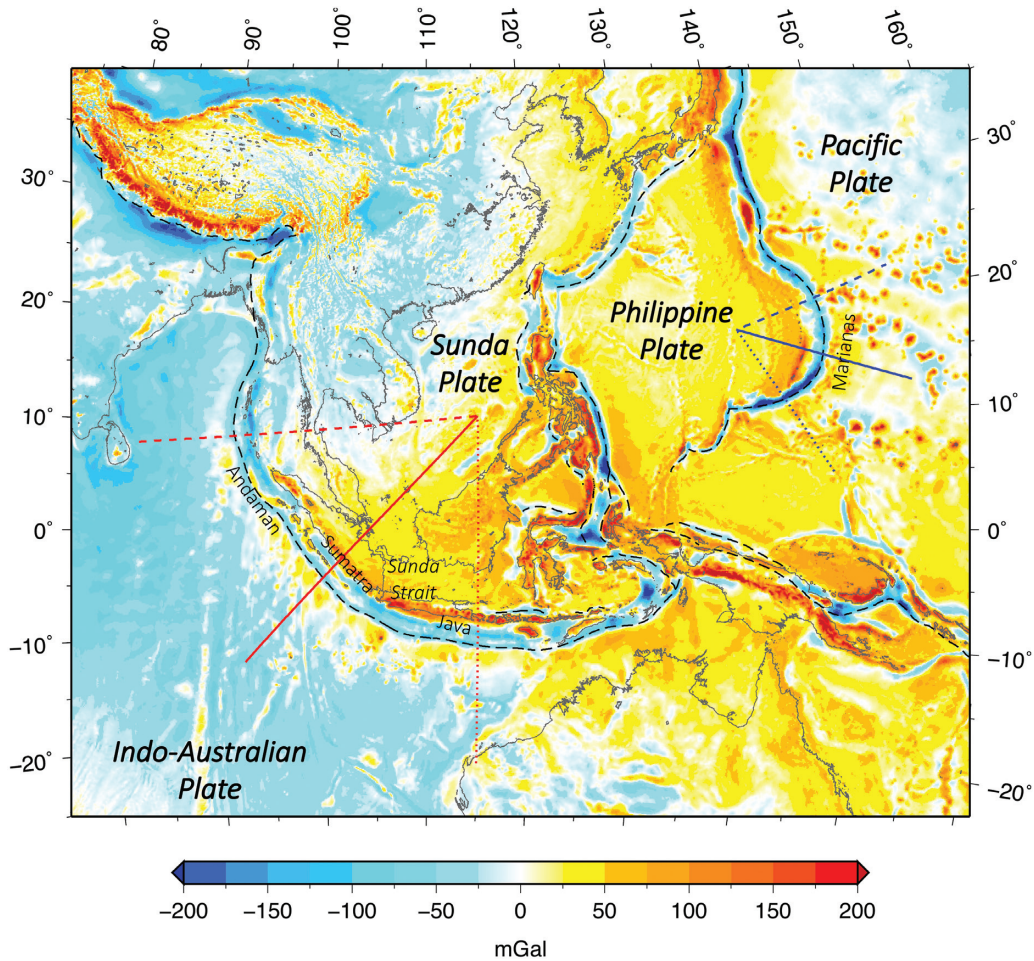
Figure 19. Gravity disturbance in the surroundings of the Sumatra and Mariana subduction complexes, computed at a height $h_S=5$ km above the ellipsoid and based on the EIGEN-6C4 model (Förste *et al.* 2014). Dashed light blue lines indicate the plate boundaries in the area.

4.3 Modelled gravity disturbance

In the previous section, we considered the density distribution at the beginning of subduction as the reference density configuration, because the target of the analysis was the perturbation induced by subduction on the gravity field. To properly compare model prediction to the EIGEN-6C4 gravity data, based on a geodetic normal Earth characterized by a uniformly thick continental crust and whose gravity is $\gamma(h, \phi)$ in eq. (8), we here define a 1-D *model normal Earth* such that it is possible to calculate a *modelled gravitational disturbance*, which is compliant with the geodetic definition of gravity disturbance given by eq. (8).

Since the *normal Earth* of the EIGEN6C4 model is based on a continental lithosphere, in order to construct the *model normal Earth*, we consider the vertical density distribution at a great distance from the trench, on the side of the continent, for all the ocean–continent models. Furthermore, since the *normal Earth* must represent the present-day reference density distribution, it is built at each time the comparison is made. Fig. 20 shows the density distribution of the model normal Earth obtained after 40 Myr from the beginning of subduction for model OC_3 that will prove to be the best-fitting model for Sumatra.

We thus calculate the *modelled gravitational disturbance* as the difference between the magnitude of the modelled gravitational contribution of the perturbed masses at a given time t, g^{model}, and the magnitude of the gravitational contribution from the *model normal Earth* at the same time t, γ^{model}, both calculated at the same point:

$$\delta g^{\mathrm{model}}(h, x, t) = g^{\mathrm{model}}(h, x, t) - \gamma^{\mathrm{model}}(h, x, t), \qquad (9)$$

where x indicates the position of the observational point with respect to the trench and h is its height above sea level. g^{model} is calculated as expressed in eqs (5) and (6), but with ρ_e instead of $\Delta\rho_e$

Among all the gravity functionals, the gravity disturbance is the most suitable one for a direct comparison with our model prediction, because it is based on the difference between the normal gravity and the actual gravity computed in the same point, without introducing any other reference point.
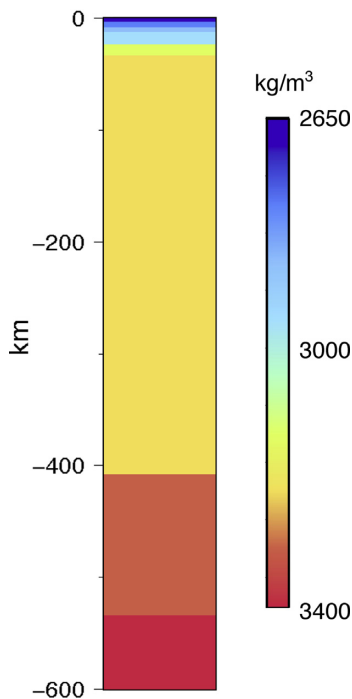
Figure 20. 1-D density distribution of the *model normal Earth* based on predictions from the OC_3 model at 40 Myr since the beginning of subduction.

4.4 Comparative analysis

4.4.1 Sumatra subduction

For the Sumatra subduction, we consider all the ocean–continent models with a subduction velocity of 5 cm yr^{-1}, compatible with the tectonic information of Section 4.1, and we calculate the gravitational contribution of the mass distribution predicted after approximately 40 Myr from the beginning of the subduction, accounting for a 4-km-thick ocean overlying the subducting plate. Below the discussion will be limited to the only model that shows the best agreement with the data, namely, model OC_3.

Panel a of Fig. 21 compares the gravity disturbance predicted by model OC_3 and the gravity disturbance based on EIGEN-6C4, extracted along three sections perpendicularly crossing the Sumatra trench in the north (dashed red line), in the centre (solid red line) and in the south (dotted red line). The model (solid black curve) based on a coupling factor of c_f=0.5 and on the bathymetry of the southern profile (Fig. 21b) fits the envelope of the profiles well in terms of positioning and height of the maxima of 30 and 200 mGal (solid red curve), with a depth of the trough or gravitational disturbance minimum of –120 mGal (dashed red curve) and with the asymptotic average values of a few tens of mGal over the subducting and overriding plates, negative and positive, respectively. As expected for a model that does not account for processes except subduction, the series of local maxima are not reproduced. Instead, the model does reproduce the narrowest trough of approximately 175–180 km of the red solid curve, evaluated from the distance between the two positive peaks surrounding the trough, to be compared in the following with that of the ocean–ocean subduction.

Panel (c) of Fig. 21 depicting the marker distribution and the density anomalies after 40 Myr since the beginning of subduction, provides the explanation for this gravitational disturbance pattern due to the narrow region of negative density contrast, as large as 80 km at most, to a depth of approximately 80 km, embedded between the subduction cold plate and the upwelled lithospheric mantle. This mantle substitutes the less dense continental crust, as indicated by the white region below the thinned crust, dark and light red in panel c of the marker distribution between 20 and 40 km, thus producing a positive density contrast, portrayed by the shallow red zone in the inset of panel (c). This shallow positive density contrast is thus effective in the thinning of the trough in the ocean–continent subduction. Furthermore, this positive density contrast has the effect of increasing the positive gravitational peak located on the continental side. This positive density contrast at depths of 20–50 km originating from the indentation of dense upper mantle material within the continental crust in this ocean–continent case to some extent shields the deeper negative density contrasts, whose contribution to the formation of the trough is thus inhibited.

4.4.2 Mariana subduction

For the Mariana subduction, we consider all the ocean–ocean models with the same value of subduction velocity of 5 cm yr^{-1} as for Sumatra, and we calculate the gravitational contribution of the mass distribution after 45 Myr, compatible with Sumatra, accounting for 5-km-thick ocean overlying the subducting plate and a 4-km-thick ocean overlying the overriding plate. Below the discussion will be limited to the only model that shows the best agreement with the data, namely, model OO_1.
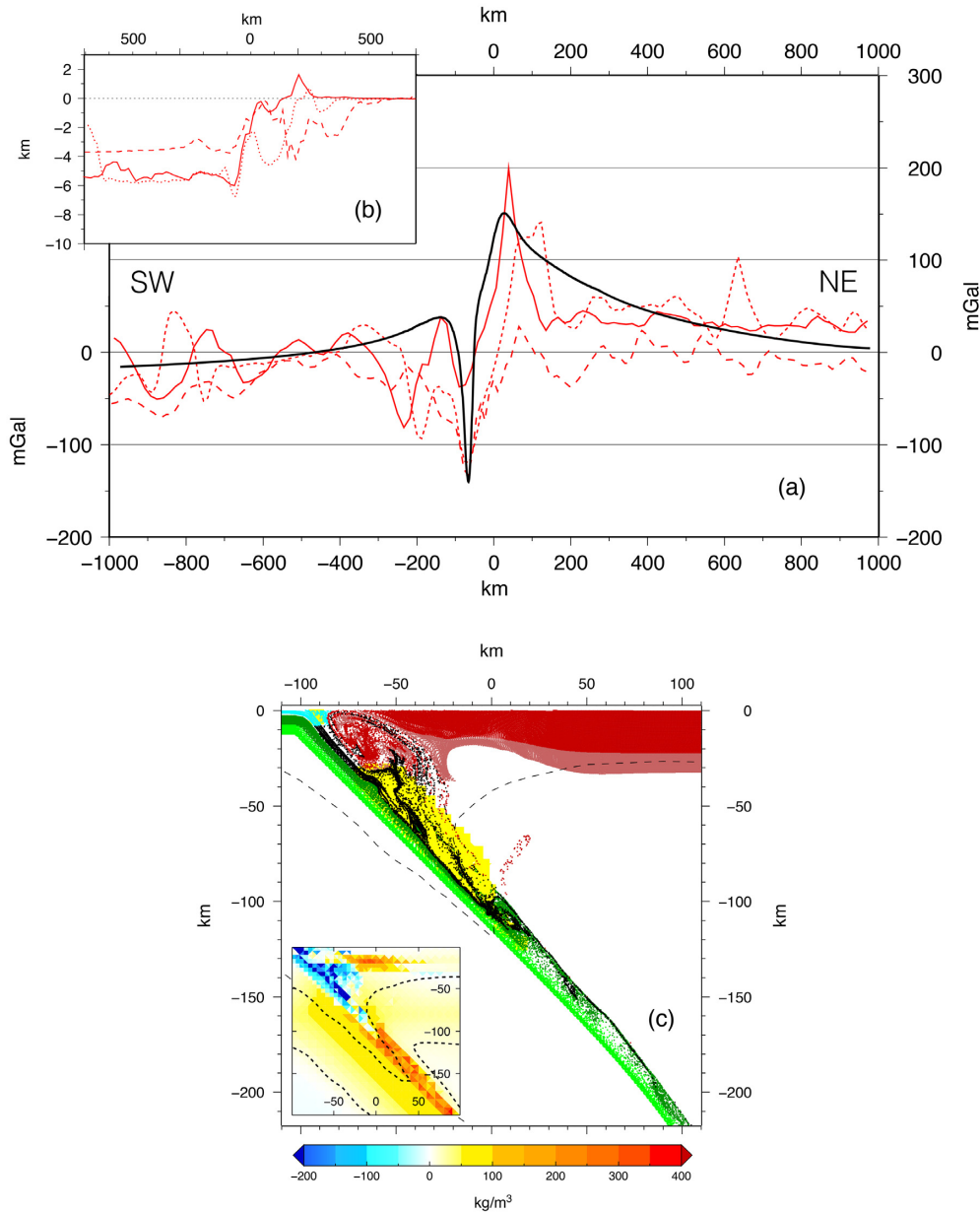
Figure 21. (a) Comparison between the gravity disturbance predicted by the OC_3 model (solid black curve) and the gravity disturbance based on the EIGEN-6C4 model, extracted along three sections crossing the Sumatra trench in the north (dashed red line), in the centre (solid red line) and in the south (dotted red line). (b) Bathymetry along the same sections as in panel a, based on the ETOPO1 1 Arc-Minute global relief model (Amante & Eakins 2009). (c) Marker distribution predicted by the OC_3 model after 40 Myr since the beginning of subduction. The insets in the panels show the density anomalies at the same times. The dashed black lines indicate the 800 and 1500 K isotherms. OC_3: $u_s = 5$ cm yr^{-1}; $\theta_s = 45°$; $c_f = 0.5$.

Fig. 22 shows the same information as Fig. 21 but for the Mariana subduction. A wider trough with respect to the ocean–continent subduction characterizes this region and is well reproduced by the OO_1 model. This model accounts for a coupling factor of $c_f = 1$ and builds on the bathymetry of the southern profile (Fig. 22, panel b). With respect to the ocean–continent subduction, the ocean–ocean subduction is also characterized by a large recirculation of light material in the mantle wedge, which is responsible for the wide region of negative density contrasts in blue in the inset of panel (c) of Fig. 22, encompassing a region in the horizontal direction as large as approximately 150 km and leading to the prediction of a large gravity trough in agreement with the data (Fig. 22a). Another major difference that makes the distribution of light material more effective in the ocean–ocean subduction in the formation of a pronounced and wide gravitational trough relies on the fact that in this type of subduction, in contrast to the ocean–continent one, the dense mantle does not substitute the lighter continental crust, which causes the formation of the positive density contrast observed above, contributing to the narrowness of the trough in the OC_3 model shown in Fig. 21.

Panel (c) of Fig. 22 provides another perspective on this issue regarding the width of the trough, showing the markers of light material well distributed along both the dip of the slab and the horizontal direction away from the trench. Thanks to the picture provided by this
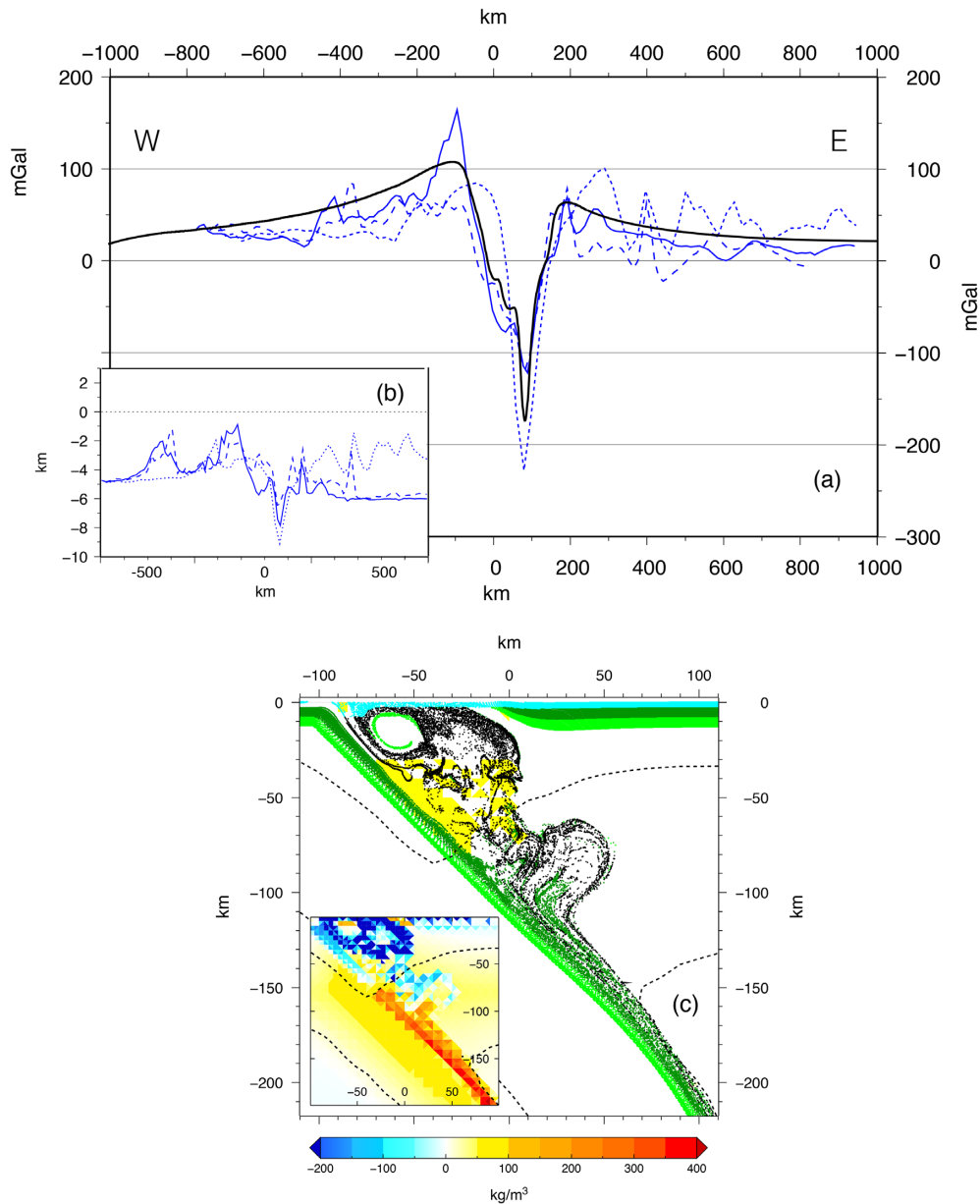
Figure 22. (a) Comparison between the gravity disturbance predicted by the OO_1 model (solid black curve) and the gravity disturbance based on the EIGEN-6C4 model, extracted along three sections crossing the Mariana trench in the north (dashed blue line), in the centre (solid blue line) and in the south (dotted blue line). (b) Bathymetry along the same sections as in panel a, based on the ETOPO1 1 Arc-Minute global relief model (Amante & Eakins 2009). (c) Marker distribution predicted by OO_1 after 45 Myr since the beginning of subduction. The insets in the panels show the density anomalies at the same times. The dashed black lines indicate the 800 and 1500 K isotherms. OO_1: $u_s = 5$ cm yr^{-1}; $\theta_s = 45°$; **$c_f = 1$**.

Figure, we can provide an explanation for other characteristics of the ocean–ocean case, namely, the second-order maxima characterizing the gravitational signature within the trough on the side of the overriding plate, both along two data profiles and along the model black curve. The recirculation of light crustal material and sediments indicated by the markers in panel (c) of Fig. 22 is characterized by a core of small-scale positive density contrast originating from the dense oceanic subducting crust, carried at shallow depth by the vigorous convective circulation occurring in the mantle wedge once out-scraped from the top of the slab. Our results allow us to provide a physical explanation for the occurrence of the small-scale local maxima in the gravitational disturbance on the side of the subducting slab due to localized dense material from the out-scraping of the slab.

5 CONCLUSIONS

We have developed a thermomechanical model that contains most of the complexities, such as compositional and phase changes, hydration, sedimentation and the degree of plate coupling, within the frame of a convective viscoplastic model, to analyse the static and time-dependent

gravitational contribution of subduction. Each of these complexities plays a role in shaping the pattern of the gravitational disturbance, particularly in the trench region, when a self-consistent comparison with EIGEN-6C4 model is also performed. The effects on the gravity pattern due to a variation of several parameters (such as the degree of plate coupling, the subduction velocity, the subduction dip and the ocean–ocean or ocean–continent environment) have been also exploited. The model results indicate that:

(i) As the plate coupling decreases, (a) the cooling of the wedge area intensifies while, at great depths, the subducted slab remains warmer; (b) the horizontal extension of the hydrated wedge area increases as the plate coupling decreases, while the maximum depth decreases; (c) the shallow negative density anomaly, associated with the trench trough, the subducted and recycled crust and sediments and the mantle hydration, increases and widens; (d) the gravitational contribution from the negative density anomalies increases as well as the amplitude of the gravity trough;

(ii) As the subduction dip angle increases: (a) the *p–T* condition becomes unfavorable for mantle hydration and recirculation of light material; (b) intense but localized shallow negative and positive density anomalies develop; (c) more intense shallow positive density anomalies while less intense deep positive density anomalies develop; (d) the gravitational contribution from the negative density anomalies decreases as well as the amplitude of the gravity trough; (e) the gravitational contribution from the positive density anomalies increases;

(iii) As the subduction velocity decreases (a) a thermal thickening of the subducted slab is enhanced at shallow depths; (b) a widespread positive density anomaly develops at the base of the upper plate and along the subducted slab; (c) the negative density anomaly is not affected by changes in the subduction velocity; (d) the gravitational contribution due to the positive density anomalies increases as well as the width of the gravity trough. When the rate of changes are normalized with respect to the corresponding subduction velocity, non-significant differences are detectable and it is possible to estimate a common rate of change of 0.008 μGal yr^{-1} (cm yr^{-1})$^{-1}$;

(iv) The differences between ocean–ocean and ocean–continent environments are due to the different dynamics within the wedge embedded between the subducting and overriding plates for the two types of subduction, affecting in particular the amount of low-density material and thus the gravity low characterizing the trough. The gravity trough is generated by the negative topography and by the low-density material that overcomes, in proximity to the trench, the global positive gravitational disturbance caused by the cold subducted lithosphere, which remains unaffected by the nature of the overriding plate, being a continent or an ocean;

(v) A gravity change of approximately 60 mGal occurs within about 2 Myr when the subducted slab crosses the *olivine-spinel* transition.

The study of the EIGEN-6C4 gravitational disturbance patterns of the Sumatra and Mariana subductions have allowed us to strengthen the analysis of the gravitational signature in ocean–continent and ocean–ocean subductions in terms of the physics of the processes occurring during the convergence of the plates. Although both types of subduction show the classical 2-D dipolar profile perpendicular to the trench, they can be distinguished in terms of some fundamental features.

Our modelling is able to reproduce the gravity disturbance difference of 250–300 mGal well between the maximum and the minimum, characterizing both types of subduction. In the same way it reproduces the fundamental differences highlighted by the EIGEN-6C4 data: (a) the width of the trough (larger for the ocean–ocean subduction than for the ocean–continent one); (b) the symmetry, in terms of the different amplitudes of the two positive gravity peaks facing the trench.

Although focused on the analysis of the different gravitational disturbance patterns of the two types of subduction, our study provides a physical explanation for the broadness of the negative gravitational contribution for mature subductions (as the Mariana) compared to immature ones, as highlighted by Kim *et al.* (2009). Serpentinization, partial melt due to frictional heating in the mantle wedge and differences in the density structure between the overriding and subducting plates were in fact proposed by Kim *et al.* (2009) to explain the broad gravitational contribution in the trench region for mature ocean–ocean subductions.

Finally, our results show that gravity patterns and their rate of change in subduction zones provide important information not only on their anomalous density structure but also on the dynamics of the subduction process, complementing those studies in which density anomalies are obtained from seismic tomography or petrological information (e.g. Kim *et al.* 2009; Simmons *et al.* 2010; Moulik & Ekström 2016).

REFERENCES

Afonso, J.C. & Ranalli, G., 2004. Crustal and mantle strengths in continental lithosphere: is the jelly sandwich model obsolete? *Tectonophysics* **394**(3–4), 221–232.

Afonso, J.C. & Zlotnik, S., 2011. The Subductability of continental lithosphere: the before and after story, in *Arc-Continent Collision,* pp. 53–86, eds Brown, D. & Ryan, P.D., Springer.

Amante, C. & Eakins, B.W., 2009. ETOPO1 1 Arc-Minute Global Relief Model: Procedures, Data Sources and Analysis. NOAA Technical Memorandum NESDIS NGDC-2, National Geophysical Data Center, NOAA, doi:10.7289/V5C8276M .

Anderson, M.O. *et al.*, 2017. Geological interpretation of volcanism and segmentation of the Mariana back–arc spreading center between 12.7° N and 18.3° N, *Geochem. Geophys. Geosyst.,* **18**(6), 2240–2274.

Arcay, D., Tric, E. & Doin, M.P., 2005. Numerical simulation of subduction zones. Effect of slab dehydration on the mantle wedge dynamics, *Phys. Earth planet. Inter.,* **149,** 133–153.

Bassett, D. & Watts, A.B., 2015a. Gravity anomalies, crustal structure, and seismicity at subduction zones: 1. Seafloor roughness and subducting relief, *Geochem. Geophys. Geosyst.,* **16**(5), 1508–1540.

Bassett, D. & Watts, A.B., 2015b. Gravity anomalies, crustal structure, and seismicity at subduction zones: 2. Interrelationships between fore–arc structure and seismogenic behavior, *Geochem. Geophys. Geosyst.,* **16**(5), 1541–1576.

Best, M.G. & Christiansen, E.H., 2001. *Igneous Petrology,* Blackwell Sci.

Bigioggero, B., Boriani, A., Colombo, A. & Gregnanin, A., 1979. The 'Diorites' of the Ivrea Basic Complexs (Central Alps, Italy), *Memorie Scienze Geologiche,* **33,** 71–85.

Billen, I.M. & Hirth, G., 2007. Rheologic controls on slab dynamics, *Geochem. Geophys. Geosyst.,* **8**(8), 1–24.

Billen, I.M., 2008. Modeling the dynamics of subducting Slabs, *Annu. Rev. Earth Planet. Sci.,* **36,** 325–356.

Blom, C.A.H., 2016, State of the art numerical subduction modeling with ASPECT; thermo-mechanically coupled viscoplastic compressible rheology, free surface, phase changes, latent heat and open sidewalls, *MSc thesis,* Utrecht University.

Borghesan, I., 2011, Impatto delle trasformazioni di fase nella dinamica del cuneo di mantello, *MSc thesis,* Universitá degli Studi di Milano.

Bradley, K.E., Feng, L., Hill, E.M., Natawidjaja, D.H. & Sieh, K., 2017. Implications of the diffuse deformation of the Indian Ocean lithosphere for slip partitioning of oblique plate convergence in Sumatra, *J. geophys. Res.,* **122**(1), 572–591.

Burg, J.-P. & Gerya, T.V., 2005. The role of viscous heating in Barrovian metamorphism of collisional Orogens: thermomechanical models and application to the Lepontine Dome in the Central Alps, *J. Metamorph. Geol.,* **23**(23), 75–95.

Castle, J.C. & Creager, K.C., 1999. A steeply dipping discontinuity in the lower mantle beneath Izu-Bonin, *J. geophys. Res.,* **104**(B4), 7279–7292.

Chopra, P.N. & Peterson, M.S., 1981. The experimental deformation of dunite, *Tectonophysics,* **78,** 453–473.

Christensen, U.R., 1992. An Eulerian Tecnique for thermo-mechanical model of lithospheric extension, *J. geophys. Res.,* **97**(B12), 2015–2036.

Christensen, U.R. & Yuen, D.A., 1985. Layered convection induced by phase transitions, *J. geophys. Res.,* **90**(B12), 10291–10300.

Connolly, J.A.D., 1990. Multivariable phase-diagrams – an algorithm based on generalized thermodynamics, *Am. J. Sci.,* **290,** 666–718.

Crameri, F. *et al.*, 2012. A comparison of numerical surface topography calculations in geodynamic modelling: an evaluation of the sticky air' method, *Geophys. J. Int.,* **189**(1), 38–54.

Dai, L., Li, S., Li, Z-.H., Somerville, I., Suo, Y., Liu, X., Gerya, T.V. & Santosh, M., 2018. Dynamics of exhumation and deformation of HP-UHP orogens in double subduction-collision systems: numerical modeling and implications for the Western Dabie Orogen, *Earth-Sci. Rev.,* **182,** 68–84.

Deer, W.A., Howie, R.A. & Zussman, J., 1992. *An Introduction to the Rock-Forming Minerals,* 2nd edn, pp. 696, Longman.

Donea, J. & Huerta, A., 2003. *Finite Element Methods for Flow Problems,* pp. 350, John Wiley & Sons.

Dubois, J. & Diament, M., 1997. *Géophysique,* Masson.

Duretz, T., Gerya, T.V. & May, D.A., 2011. Numerical modelling of spontaneous slab breakoff and subsequent topographic response, *Tectonophysics,* **502,** 244–256.

Faccenda, M., Gerya, T.V. & Burlini, L., 2009. Deep slab hydration induced by bending-related variations in tectonic pressure, *Nat. Geosci.,* **1**(11), 790–793.

Faccenda, M. & Mancktelow, N.S., 2010. Fluid flow during unbending: implications for slab hydration, intermediate-depth earthquakes and deep fluid subduction, *Tectonophysics,* **494**(1-2), 149–154.

Faccenda, M., 2014. Water in the slab: a trilogy, *Tectonophysics,* **614,** 1–30.

Faccenna, C., Holt, A.F., Becker, T.W., Lallemand, S. & Royden, L.H., 2018. Dynamics of the Ryukyu/Izu-Bonin-Marianas double subduction system, *Tectonophysics,* **746,** 229–238.

Fei, Y. *et al.*, 2004. Experimentally determined postspinel transformation boundary in Mg_2SiO_4 using MgO as an internal pressure standard and its geophysical implications, *J. geophys. Res.,* **109,** B02305.

Förste, C. *et al.*, 2014. EIGEN-6C4 The latest combined global gravity field model including GOCE data up to degree and order 2190 of GFZ Potsdam and GRGS Toulouse, *IGFZ Data Services,* doi:10.5880/icgem.2015.1.

Gamage, S.S.N., 2017. Seismic activity near the Sunda and Andaman Trenches in the Sumatra subduction zone, *Int. J. Multidiscip. Stud.,* **4**(2), doi:10.4038/ijms.v4i2.22 .

Gerya, T.V., Stockhert, B. & Perchuk, A.L., 2002. Exhumation of high-pressure metamorphic rocks in a subduction channel: a numerical simulation, *Tectonics,* **21**(6), 1–15.

Gerya, T.V. & Yuen, D.A., 2003. Rayleigh–Taylor instabilities from hydration and melting propel 'cold plumes' at subduction zones, *Earth planet. Sci. Lett.,* **212**(1–2), 47–62.

Gerya, T.V., Yuen, D.A. & Maresch, W.V., 2004. Thermomechanical modelling of slab detachment, *Earth planet. Sci. Lett.,* **226**(6), 101–116.

Gerya, T.V. & Stockhert, B., 2006. Two-dimensional numerical modeling of tectonic and metamorphic histories at active continental margins, *Int. J. Earth Sci. (Geol. Rundsch.*), **95**(2), 250–274.

Gerya, T., 2010. *Numerical Geodynamic Modelling,* pp. 345, Cambridge Univ. Press.

Gerya, T.V., 2015. Tectonic overpressure and underpressure in lithospheric tectonics and metamorphism, *J. Metamorphic Geol.,* **33,** 785–800.

Gorczyk, W., Gerya, T.V., Connolly, J.A.D., Yuen, D.A. & Rudolph, M., 2006. Large-scale rigid-body rotation in the mantle wedge and its implications for seismic tomography, *Geochem. Geophys. Geosyst.,* **7**(5), 1–23, Q05018, doi:10.1029/2005GC001075.

Gurnis, M. & Hager, B.H., 1988. Controls of the structure of subducted slabs, *Nature,* **335**(6188), 317.

Haenel, R., Rybach, L. & Stegena, L., 1988. *Handbook of Terrestrial Heat-Flow Density Determination,* Kluwer Academic Publishers.

Hager, B.H., O'Connell, R.J & Raefsky, A., 1983. Subduction, back-arc spreading and global mantle flow, *Tectonophysics,* **99**(2–4), 165–189.

Hager, B.H., 1984. Subducted slabs and the geoid: constraints on mantle rheology and flow, *J. geophys. Res.,* **89**(B7), 6003–6015.

Hall, R., Fuller, M., Ali, J.R. & Anderson, C.D., 1995. The Philippine Sea plate: magnetism and reconstructions, *Active Margins Marginal Basins Western Pacific,* **88,** 371–404.

Holt, A.F., Royden, L.H., Becker, T.W. & Faccenna, C., 2018. Slab interactions in 3-D subduction settings: The Philippine Sea Plate region, *Earth planet. Sci. Lett.,* **489,** 72–83.

Honda, S. & Saito, M., 2003. Small-scale convection under the back-arc occurring in the low viscosity wedge, *Earth planet. Sci. Lett.,* **216,** 703–715.

Hughes, T.J.R., Liu, W. & Brooks, A., 1979. Finite element analysis of Incompressible viscous flows by the penalty function formulation, *J. Comp. Phys.,* **30,** 1–60.

Ismail-Zadeh, A. & Tackley, P., 2010. *Computational Methods for Geodynamics,* pp. 313, Cambridge Univ. Press.

Jungels, P.H., 1973, Models of tectonic processes associated with earthquakes, *PhD thesis,* pp. 207, California Institute Technology, Pasadena, California.

Jungels, P.H. & Frazier, G.A., 1973. Finite element analysis of the residual displacements for an earthquake rupture: source parameters for the San Fernando earthquake, *J. geophys. Res.,* **78,** 5062–5083.

Katsura, T. & Ito, E., 1989. The system Mg2SiO4-Fe2SiO4 at high pressures and temperatures: precise determination of stabilities of olivine, modified spinel, and spinel, *J. geophys. Res.,* **94,** 15 663–15 670.

Kerschhofer, L., Dupas, C., Liu, M., Sharp, T.G., Durham, W.B. & Rubie, D.C., 1998. Polymorphic transformations between olivine, wadsleyite and ringwoodite: mechanisms of intracrystalline nucleation and the role of elastic strain, *Mineral. Mag.,* **62**(5), 617–638.

Kim, Y.M., Lee, S.M. & Okino, K., 2009. Comparison of gravity anomaly between mature and immature intra-oceanic subduction zones in the western Pacific, *Techtonophysics,* **474,** 657–673.

Kirby, S.H., 1983. Rheology of the lithosphere, *Rev. Geophys.,* **21**(6), 1459–1487.

Kong, X., Li, S., Wang, Y., Suo, Y., Dai, L., Geli, L., Zhang, Y., Guo, L. & Wang, P., 2018. Causes of earthquake spatial distribution beneath the Izu-Bonin-Mariana Arc, *J. Asian Earth Sci.,* **151,** 90–100.

Kundu, B. & Gahalaut, V.K., 2011. Slab detachment of subducted Indo-Australian plate beneath Sunda arc, Indonesia, *J. Earth Syst. Sci.,* **120**(2), 193–204.

Liu, L., Zhang, J., Green, H.W., Jin, Z. & Bozhilov, K.N., 2007. Evidence of former stishovite in metamorphosed sediments, implying subduction to > 350 km, *Earth planet. Sci. Lett.,* **263,** 180–191.

Malod, J.A. & Kemal, B.M., 1996. The Sumatra margin: oblique subduction and lateral displacement of the accretionary prism, *Geol. Soc., Lond., Spec. Publ.,* **106**(1), 19–28.

Marotta, A.M., Spelta, E. & Rizzetto, C., 2006. Gravity signature of crustal subduction inferred from numerical modelling, *Geophys. J. Int.,* **166,** 923–938.

Marotta, A.M., Barzaghi, R., Borghi, A. & Spelta, E., 2007. Gravity constraints on the dynamics of the crust–mantle system during Calabrian subduction, *Geophys. J. Int.,* **171,** 977–985.

Marotta, A.M., Roda, M., Conte, K. & Spalla, M.I., 2018. Thermomechanical numerical model of the transition from continental rifting to oceanic spreading: the case study of the Alpine Tethys, *Geol. Mag.,* **155**(2), 250–279.

Melosh, H.J. & Raefsky, A., 1980. The dynamical origin of subduction zone topography, *J. geophys. Int.,* **60**(3), 333–354.

Melosh, H.J. & Raefsky, A., 1981. A simple and efficient method for introducing faults into finite element computations, *Bull. seism. Soc. Am.,* **71**(5), 1391–1400.

Miller, M.S., Gorbatov, A. & Kennett, B.L.N., 2005. Heterogeneity within the subducting Pacific slab beneath the Izu–Bonin–Mariana arc: evidence from tomography using 3D ray tracing inversion techniques, *Earth planet. Sci. Lett.,* **235**(1–2), 331–342.

Miller, M.S., Gorbatov, A. & Kennett, B.L., 2006. Three-dimensional visualization of a near-vertical slab tear beneath the southern Mariana arc, *Geochem. Geophys. Geosyst.,* **7**(6), doi:10.1029/2005GC001110 .

Moeremans, R., Singh, S.C., Mukti, M., McArdle, J. & Johansen, K., 2014. Seismic images of structural variations along the deformation front of the Andaman–Sumatra subduction zone: implications for rupture propagation and tsunami genesis, *Earth planet. Sci. Lett.,* **386,** 75–85.

Moulik, P. & Ekström, G., 2016. The relationships between large-scale variations in shear velocity, density, and compressional velocity in the Earth's mantle, *J. geophys. Res.,* **121,** 2737–2771.

Negredo, A.M., Valera, J.L. & Carminati, E., 2004. TEMSPOL: a MATLAB thermal model for deep subduction zones including major phase transformations, *Comput. Geosci.,* **30,** 249–258.

Nielsen, C., Chamot-Rooke, N. & Rangin, C., 2004. From partial to full strain partitioning along the Indo-Burmese hyper-oblique subduction, *Marine Geology,* **209**(1–4), 303–327.

Oberhansli, R., Hunziker, J.C., Martinotti, G. & Stern, W.B., 1985. Geochemistry, geochronology and petrology of Monte Mucrone: an example of EO-alpine eclogitization of Permian granitoids in the Sesia- Lanzo Zone, Western Alps, Italy, *Chem. Geol.,* **52**(2), 165–184.

Origoni, E.G. & Gregnanin, A., 1983. The cristalline basement of the Massiccio delle Tre Valli Bresciane: new petrographic and chemical data, *Memorie della Societá Geologica Italiana,* **26,** 133–144.

Pearce, J.A., Reagan, M.K., Petronotis, K., Morgan, S., Almeev, R., Avery, A.J. & Godard, M., 2015. Izu-Bonin-Mariana fore arc: Testing subduction initiation and ophiolite models by drilling the outer Izu-Bonin-Mariana fore arc; 30 July–29 September 2014, *Integrated Ocean Drilling Program: Expedition 352 Preliminary Reports,* **352,** doi:10.14379/iodp.pr.352.2015 .

Perez-Gussinye, M. & Reston, T.J., 2001. Rheological evolution during extension at nonvolcanic rifted margins: onset of serpentinization and development of detachments leading to continental breakup, *J. geophys. Res.,* **106**(B3), 3961–3975.

Perry, M., Spinelli, G.A., Wada, I. & He, J., 2016. Modeled temperatures and fluid source distributions for the Mexican subduction zone: effects of hydrothermal circulation and implications for plate boundary seismic processes, *Geochem. Geophys. Geosyst.,* **17,** 550–570.

Quinquis, M.E.T. & Buiter, S.J.H., 2014. Testing the effects of basic numerical implementations of water migration on models of subduction dynamics, *J. geophys. Res.,* **5**(1), 537–555.

Ranalli, G. & Murphy, D.C., 1987. Rheological stratification of the lithosphere, *Tectonophysics,* **132**(4), 281–295.

Regorda, A., Roda, M., Marotta, A.M. & Spalla, M.I., 2010. 2-D numerical study of hydrated wedge dynamics from subduction to post-collisional phases, *Geophys. J. Int.,* **211,** 952–978.

Roda, M., Marotta, A.M. & Spalla, M.I., 2010. Numerical simulations of an ocean–continent convergent system: Influence of subduction geometry and mantle wedge hydration on crustal recycling, *Geochem. Geophys. Geosyst.,* **11**(5), 1–21.

Roda, M., Marotta, A.M. & Spalla, M.I., 2011. The effects of the overriding plate thermal state on the slab dip in an ocean–continent subduction system, *Compte Rendu Academie des Sciences Paris,* **343**(5), 323–330.

Roda, M., Spalla, M.I. & Marotta, A.M., 2012. Integration of natural data within a numerical model of ablative subduction: a possible interpretation for the Alpine dynamics of the Austroalpine crust, *J. Metamor.,* **30**(9), 973–996.

Rosas, J.C., Currie, C.A., Harris, R.N. & He, J., 2016. Effect of hydrothermal circulation on slab dehydration for the subduction zones of Costa Rica and Nicaragua, *Phys. Earth planet. Inter.,* **255,** 66–79.

Rupke, L.H., Morgan, J.P., Hort, M. & Connolly, J.A., 2004. Serpentine and the subduction zone water cycle, *Earth planet. Sci. Lett.,* **223**(1-2), 17–34.

Rupke, L.H., Schmid, D.W., Perez-Gussinye, M. & Hartz, E., 2013. Interrelation between rifting, faulting, sedimentation, and mantle serpentinization during continental margin formation- including examples from the Norwegian Sea, *Geochem. Geophys. Geosyst.,* **14**(10), 4351–4369.

Ruh, J.B., Gerya, T. & Burg, J.P., 2013. High-resolution 3D numerical modeling of thrust wedges: influence of décollement strength on transfer zones, *Geochem. Geophys. Geosyst.,* **14**(4), 1131–1155.

Schilling, J.G., Zajac, M., Evans, R., Johnston, T., White, W.M., Devine, J.D. & Kingsley, R., 1983. Petrologic and geochemical variations along the Mid-Atlantic Ridge from 29°N to 73°N, *Am. J. Sci.,* **283,** 510–586.

Schluter, H.U., Gaedicke, C., Roeser, H.A., Schreckenberger, B., Meyer, H., Reichert, C., Djajadihardja, Y. & Prexl, A., 2002. Tectonic features of the southern Sumatra-western Java forearc of Indonesia, *Tectonics,* **21**(5).

Schmeling, H. *et al.*, 2008. A benchmark comparison of spontaneous subduction models—towards a free surface, *Phys. Earth planet. Inter.,* **171,** 198–223.

Schmidt, M.W. & Poli, S., 1998. Experimentally based water budgets for dehydrating slabs and consequences for arc magma generation, *Earth planet. Sci. Lett.,* **163,** 361–379.

Sdrolias, M., Roest, W.R. & Müller, R.D., 2004. An expression of Philippine Sea plate rotation: the Parece Vela and Shikoku basins, *Tectonophysics,* **394**(1–2), 69–86.

Sewell, G., 1981. Twodepep: a small general purpose finite element program, IMSL Technical Report Series 8102.

Shapiro, N.M., Ritzwoller, M.H. & Engdahl, E.R., 2008. Structural context of the great Sumatra-Andaman Islands earthquake, *Geophys. Res. Lett.,* **35**(L05301), doi:10.1029/2008GL033381.

Silvestrin, P., Aguirre, M., Massotti, L., Leone, B., Cesare, S., Kern, M. & Haagmans, R., 2012. The future of the satellite gravimetry after the GOCE mission, *Int. Asseoc. Geodesy Symp.,* **136,** 223–230.

Simmons, N.A., Forte, A.M., Boschi, L. & Grand, S.P., 2010. GyPSuM: a joint tomographic model of mantle density and seismic wave speeds, *J. geophys. Res.,* **115,** 1–24.

Stern, R.J. & Gerya, T.V., 2018. Subduction initiation in nature and models: a review, *Tectonophysics,* **746,** 173–198.

Syracuse, E.M. & Abers, G.A., 2006. Global compilation and variations in slab depth beneath arc volcanoes and implications, *Geochem. Geophys. Geosyst.,* **7**(5), 1–18.

Thielmann, M. & Kaus, B., 2012. Shear heating induced lithospheric-scale localization: does it result in subduction? *Earth planet. Sci. Lett.,* **359-360,** 1–13.

Thieulot, C., 2014. Elefant: a user-friendly multipurpose geodynamics code, *J. geophys. Res.,* **6,** 1949–2096.

Turcotte, D.L. & Schubert, G., 2002. *Geodynamics,* 2nd edn, pp. 345, Cambridge Univ. Press.

Yamato, P., Agard, P., Burov, E., Pourhiet, L.L., Jolivet, L. & Tiberi, C., 2007. Burial and exhumation in a subduction wedge: mutual constraints from thermomechanical modeling and natural P-T-t data (Schistes Lustrés, western Alps), *J. geophys. Res.,* **112,** 1–28.

van der Hilst, R. & Seno, T., 1993. Effects of relative plate motion on the deep structure and penetration depth of slabs below the Izu-Bonin and Mariana island arcs, *Earth planet. Sci. Lett.,* **120**(3-4), 395–407.

van Hunen, J., van den Berg, A.P. & Vlaar, N.J., 2001. Latent heat effects of the major mantle phase transitions on low-angle subduction, *Earth planet. Sci. Lett.,* **190,** 125–135.

Wang, S., Yu, H., Zhang, Q. & Zhao, Y., 2018. Absolute plate motions relative to deep mantle plumes, *Earth planet. Sci. Lett.,* **490,** 88–99.

Wang, Y., Zhang, L.F., Li, Z.H., Li, Q.Y. & Bader, T., 2019. The exhumation of subducted oceanic derived eclogites: insights from phase equilibrium and thermomechanical modeling, *Tectonics,* **38,** doi:10.1029/2018TC005349.

Watts, A.B. & Talwani, M., 1974. Gravity anomalies seaward of deep-sea trenches and their tectonic implications, *J. geophys. Int.,* **36**(1), 57–90.

Wessel, P., Smith, W.H.F., Scharroo, R., Luis, J.F. & Wobbe, F., 2013. Generic mapping tools: improved version released, *EOS, Trans. Am. Geophys. Un.,* **94**(45), 409–410.

Zhong, S. & Gurnis, M., 1992. Viscous flow model of a subduction zone with a faulted lithosphere: long and short wavelength topography, gravity and geoid, *Geophys. Res. Lett.,* **19**(18), 1891–1894.

Zhong, S. & Gurnis, M., 1994. Controls on trench topography from dynamic models of subducted slabs, *J. geophys. Res,* **99**(15), 15 683–15 695.

APPENDIX A: MATHEMATICAL FORMULATION

The eqs (1), (2) and (3) are numerically integrated via the 2-D FE thermomechanical code *SubMar* (Marotta *et al.* 2006), which uses the Petrov–Galerkin method to integrate the conservation of energy equation and the penalty formulation:

$$p = -\lambda \left(\frac{\partial u}{\partial x} + \frac{\partial v}{\partial y} \right) \tag{A1}$$

to solve for pressure, where λ is the penalty parameter. We follow Sewell (1981)'s approach and fix $\lambda = \mu \sqrt{r_p}$, where r_p denotes the machine relative precision and μ is interpreted as a bulk viscosity (Hughes *et al.* 1979; Donea & Huerta 2003; Marotta *et al.* 2006; Thieulot 2014). The marker-in-cell technique (e.g., Christensen 1992) has been used to compositionally differentiate the different types of materials. At the beginning of the evolution, 455 489 markers identified by different code are spatially distributed, with a density of 1 marker per 0.25 km², to define the upper and lower oceanic crust, the upper and lower continental crust and the continental mantle. During the evolution of the system, each particle (marker) is advected using a fourth-order (both in time and in space) Runge–Kutta scheme. At each time, the elemental density of each type of particle defines the composition of each element of the grid, C^e, such as

$$C^e = \sum_i C_i^e, \tag{A2}$$

where

$$C_i^e = \frac{N_i^e}{N_0^e}, \tag{A3}$$

where N_i^e and N_0^e are the number of particles of type i within element e and the maximum number of particles of any type that the element e contains, respectively. Each elemental property P^e (conductivity, specific heat at a constant pressure, density and viscosity) depends on the composition such that within each element e, P^e can be expressed as follows:

$$P^e = P_m \left[1 - \sum_i C_i^e \right] + \sum_i P_i C_i^e, \tag{A4}$$

where P_m and P_i are the property for mantle and for any particles of type i, respectively. For what concerns the density, if it depends only on temperature, the corresponding variations are generally small, and the fluid can be assumed to be incompressible. The density can consequently be treated as a constant in the continuity (1) and energy eq. (3), leading to an incompressible fluid (e.g. Christensen & Yuen 1985; Ismail-Zadeh & Tackley 2010). If density variations depend not only on temperature variations but also on pressure variations as considered herein, then compressibility must be taken into account. Accounting for compressibility can be achieved by using either the extended Boussinesq approximation or the anelastic approximation (Gerya 2010; Ismail-Zadeh & Tackley 2010). Here, we implemented the extended Boussinesq approximation in the following form:

$$\rho(T, C, p) = \rho_m \left[1 - \sum_i C_i \right] + \sum_i \rho_i C_i, \tag{A5}$$

where $\rho_m(T, p)$ is the mantle density; $\rho_i(T, p)$, with i varying from 1 to the total number of no-mantle material types included in the model, are the densities of no-mantle material (e.g., Ismail-Zadeh & Tackley 2010; Thielmann & Kaus 2012; Quinquis & Buiter 2014; Thieulot 2014); and C_i are the corresponding compositions. Both ρ_m and ρ_i are functions of temperature, pressure and material type. The extended Boussinesq approximation allows us to consider the density as a constant in the continuity eq. (1), while it accounts for density variations in the buoyancy term of the momentum eq. (2) and for both the shear and adiabatic heating terms in the energy eq. (3), where the

Table A1. Values of the material and rheological parameters used in the analysis. References: (a) Ranalli & Murphy (1987); (b) Afonso & Ranalli (2004); (c) Kirby (1983); (d) Haenel *et al.* (1988); (e) Chopra & Peterson (1981); (f) Dubois & Diament (1997) and Best & Christiansen (2001); (g) Roda *et al.* (2011); (h) Schmidt & Poli (1998); (i) Gerya & Stockhert (2006); (j) Roda *et al.* (2012); (k) Gerya & Yuen (2003); (l) Borghesan (2011); (m) Schmeling *et al.* (2008). pc: Perple$_X$ derived.

		Continental crust		Oceanic crust		Sediments	Mantle	Serpentine	Air	Water
		Upper	Lower	Upper	Lower					
Lithology										
		Granite	Diorite	N-MORB		Mica-schists	Dunite	Serpentine		
				Mid-Atlantic Ridge						
Density	ρ (kg · m^{-3})	pc	pc	pc		pc	pc	3000	1.18	1000
Conductivity	K (W · m^{-1} · K^{-1})	3.03		2.1		3.03	4.15	4.15	0.026	0.600
Heat production	H (μW · m^{-3})	2.5		0.4		2.5	0.002	0.002	0	0
Rheology										
		Dry granite		Dry diabase		Dry granite	Dry dunite	Serpentinite	Sticky air/water	
Activation energy	E (kJ · mol^{-1})	38.4		103.2	103.2	38.4	130.2	0	0	
Reference viscosity	μ_0 (Pa · s)	3.47· 10^{21}		1.61· 10^{19}	1.61· 10^{22}	3.47· 10^{20}	5· 10^{20}	10^{19}	10^{19}	
Based on		a, d, f, l		a, b, c, f, l	a, b, c, f, l	a, d, f, l	c, d, e, f, j	d, f, g, h, i	m	

internal heating per mass unit can be expressed as follows:

$$H = H_r + H_s + H_a, \tag{A6}$$

where H_r is the radiogenic heating, $H_s = \tau_{ij}\dot\epsilon$ is the shear heating and $H_a = T\alpha\frac{Dp}{Dt}$, where α is the thermal expansion coefficient, is the adiabatic heating per mass unit (e.g. Christensen & Yuen 1985; Gerya 2010; Ismail-Zadeh & Tackley 2010; Thielmann & Kaus 2012).

The extended Boussinesq approximation is widely used when dealing with compressible fluids (Gerya *et al.* 2004; Burg & Gerya 2005; Gorczyk *et al.* 2006; Duretz *et al.* 2011; Wang *et al.* 2019) accounting for changes in the buoyancy term due to density changes in the momentum and in the energy equations, including those from phase transformations, and for a time-invariant density in the continuity equation (Ismail-Zadeh & Tackley 2010). In order to enforce locally and only for lithospheric material the mass conservation where phase changes occur, Afonso & Zlotnik (2011) introduced in the momentum equation the contribution from the divergence of the velocity field obtained by approximating the continuity equation according to $\partial u/\partial x + \partial v/\partial y \simeq -(1/\rho)(\triangle\rho/\triangle t)$.

$\triangle\rho$ denotes in each Lagrangian particle the difference between the density in the current and previous time step, which generates a localized velocity field that compresses or expands the material at the time of the phase transition in the lithosphere, enforcing locally the mass conservation and providing a higher order approximation within the scheme of the extended Bousinnesq approximation. We also account for the changes in time of the density due to phase changes, by modifying at each time step the current density according to the pressure and temperature conditions, as required by the extended Bousinessq approximation, both in the buoyancy term of the momentum equation and in the energy equations, as described in Appendix C. In our model mass conservation is guaranteed in the study domain by the horizontal material flow in and out of the domain across its vertical left boundary, as shown in Fig. 2. The model combines a linear viscous rheology for the sublithospheric mantle with a linear viscoplastic rheology for the lithosphere. To this purpose, for each material type i, we compute the following two viscosities:

$$\mu_i^{\text{viscous}} = \mu_{0,i} \cdot e^{\left[\frac{E_i}{R}\left(\frac{1}{T} - \frac{1}{T_0}\right)\right]}, \tag{A7}$$

where $\mu_{0,i}$ and E_i are the reference viscosity at the reference temperature T_0 and the activation energy, respectively, for material type i

$$\mu^{\text{plastic}} = \min\left[\mu_1, \mu_2, \mu_3\right] \tag{A8}$$

with μ_1, μ_2 and μ_3 computed combining the Byerlee's law criterion and the Tresca criterion as implemented in Regorda *et al.* (2017)

$$\mu_1 = \frac{\sigma_Y - p}{2\dot\epsilon_1}; \qquad \mu_2 = \frac{\sigma_Y - p}{2\dot\epsilon_2}; \qquad \mu_2 = \frac{\sigma_Y}{2(\dot\epsilon_1 - \dot\epsilon_2)}, \tag{A9}$$

where p is the pressure, $\dot\epsilon_1$, $\dot\epsilon_2$ and $\dot\epsilon_3$ are the principal strain rates and σ_Y is the yield stress, defined by the simplified formulation of Byerlee's law criterion, $\sigma_Y = \beta \cdot y$, with $\beta = 40$ MPa km^{-1} and y depth in kilometres. Outside the lithosphere, the effective viscosity is then calculated as follows:

$$\mu^{\text{effective}} = \mu_{\text{viscous}}. \tag{A10}$$

Within the lithospheric layer the effective viscosity is instead defined as follows:

$$\mu^{\text{effective}} = \min\left[\mu_i^{\text{viscous}}, \mu_i^{\text{plastic}}\right]. \tag{A11}$$

Table A1 lists the values of the material and rheological parameters used in the analysis. Instantaneous erosion/sedimentation mechanism is simulated as in Roda *et al.* (2010) by using the substitution technique, in which all the crustal particles lying above a prescribed height (h_t in Table 1) are replaced with air particles and, at the same time, an equal number of water particles buried into the trench region are transformed

into sediments. This procedure reproduces an erosion and sedimentation rate variable in time, as function of the system dynamics. Further details can be found in (Roda *et al.* 2010)

APPENDIX B: HYDRATION AND SERPENTINIZATION OF THE WEDGE AREA

Water contained in hydrous phases in H_2O-saturated MORB basalt can be transported to large depths (e.g. Liu *et al.* 2007; Faccenda 2014; Rosas *et al.* 2016), where the oceanic plate is then dehydrated because of the increased temperature and pressure (Schmidt & Poli 1998; Liu *et al.* 2007; Faccenda *et al.* 2009; Faccenda & Mancktelow 2010). Schmidt & Poli (1998) and Liu *et al.* (2007) suggested that complete dehydration is achieved at a depth between 70 and 350 km. Furthermore, Faccenda *et al.* (2009), Faccenda & Mancktelow (2010) and Faccenda (2014) showed that tectonic stresses can influence the hydration pattern in the subducted slab, allowing fluids to penetrate into the slab and favouring their transport to great depths up to the base of the upper mantle. The presence of hydrothermal circulation in the oceanic crust can affect the thermal state in the subducting slab, which generates higher hydrous phase stability at higher depths compared with those predicted by classical thermal models of the subduction zone (Perry *et al.* 2016; Rosas *et al.* 2016). However, hydrothermal circulation does not have a significant impact on the depth of dehydration reactions at shallow depths (Rosas *et al.* 2016).

The phases with large contributions to the water budget of subducting MORB are lawsonite, chlorite and amphibole; however, at pressures higher than 3–4 GPa, lawsonite constitutes the only hydrous phase. At pressures above the zoisite stability field, the lawsonite breakdown reaction has a positive dp/dT slope in the coesite stability field, while it has a negative dp/dT slope in the stishovite stability field, above 8 GPa (Schmidt & Poli 1998). In our models, the maximum dehydration depth of the oceanic crust, below which the water content in the subducting oceanic plate is negligible, has been determined using the stability field of lawsonite as follows:

$$p_{dehydr} = -\frac{1.8}{335} \cdot (T_{marc} - 773) + 10 \quad \text{above} \quad 8 \text{ GPa} \tag{B1}$$

$$p_{dehydr} = +\frac{5}{155} \cdot (T_{marc} - 1108) + 8.2 \quad \text{below} \quad 8 \text{ GPa}, \tag{B2}$$

where p_{dehydr} is the maximum pressure at which lawsonite is stable calculated for each oceanic crustal marker with temperature T_{marc}.

The water released by the slab hydrates the mantle wedge and can lead to its serpentinization, with a consequent decrease in viscosity and density (Honda & Saito 2003; Gerya *et al.* 2002; Arcay *et al.* 2005). The rheological weakening of the mantle wedge has been simulated by assuming a constant viscosity of 10^{19} Pa · s and a density of 3000 kg m^{-3} for the serpentinized mantle (Honda & Saito 2003; Arcay *et al.* 2005; Gerya & Stockhert 2006; Roda *et al.* 2010).

In our models, the stability field of serpentine is calculated for each element as follows:

$$p_{hydr} = -\frac{8}{300} \cdot (T_{elem} - 1093) \quad \text{above} \quad 2 \text{ GPa} \tag{B3}$$

$$p_{hydr} = +\frac{5.4}{600} \cdot (T_{elem} - 773) \quad \text{below} \quad 2 \text{ GPa}, \tag{B4}$$

where p_{hydr} represents the maximum pressure at which serpentine is stable at the elemental temperature T_{elem}. The hydrated area is limited from below by the oceanic subducting plate. Specifically, to better delineate the geometry of the lower border of the hydrated area, the subducted plate is subdivided into segments of equal length, and the deepest dehydrated oceanic crust marker for each segment is identified at each time during the system's dynamic evolution. The line that connects these markers defines the lower limit of the hydrated area.

We implement a free-water migration mechanism at a constant velocity of 20 cm yr^{-1}, in accordance with the velocities obtained by Quinquis & Buiter (2014) for different water migration schemes (10–70 cm yr^{-1}). Further, Quinquis & Buiter (2014) demonstrated that the exact manner of water migration does not impact the dynamics in the mantle wedge. We also assume that the used time step (50 000 yr) is sufficient to have a complete serpentinization of the hydrated areas (Arcay *et al.* 2005).

APPENDIX C: PHASE CHANGES

In all models, the phase changes were introduced both for the mantle and for all the lithologies considered for the crust. For each phase change, we introduced density variations in relation to the variation in pressure and temperature (*p–T*) conditions predicted by the models.

Regarding the phase changes occurring in the mantle, Fig. C1 shows the assumed stability fields for olivine, wadsleyite, ringwoodite and perovskite+periclase. Considering a temperature of ∼1600 K for the upper mantle, olivine is expected to transform into wadsleyite at a pressure of ∼13 GPa, while the wadsleyite → ringwoodite transformation is expected to occur at ∼17.5 GPa (Katsura & Ito 1989; Kerschhofer *et al.* 1998), both with a positive Clapeyron slope. We considered a density for the olivine of 3200 kg m^{-3} (Deer *et al.* 1992), while the $\alpha \rightarrow \beta$ and $\beta \rightarrow \gamma$ phase transformations result in increases in density of 6 and 2 per cent (Kerschhofer *et al.* 1998), respectively, obtaining densities of 3392 and 3460 kg m^{-3} for the wadsleyite and ringwoodite, respectively. At the bottom of the upper mantle, ringwoodite transforms into perovskite + periclase ($MgSiO_3 + MgO$). At a temperature of 1600 K, this transformation occurs at ∼22 GPa (corresponding to the 660-km seismic velocity discontinuity in the mantle), with a negative Clapeyron slope (Fei *et al.* 2004) and refs. therein), and produces an additional increase in density. In particular, considering densities of ∼4000 and ∼3600 kg m^{-3} for the perovskite and the periclase (Deer *et al.* 1992), respectively, we assumed a density of 3800 kg m^{-3} for the lower mantle.

In contrast, Perple$_X$ (Connolly 1990) has been used to introduce density variations related to multiple phase changes occurring at the same time in the oceanic crust and continental crust and in the sediments, each characterized by particular bulk compositions (Borghesan 2011):

(i) the oceanic crust has the bulk composition of a mid-Atlantic ridge N-MORB (Schilling *et al.* 1983);
(ii) the continental crust has been separated into the upper crust, with the bulk composition of the Mucrone granite (Oberhansli *et al.* 1985), and the lower crust, with the bulk composition of the Ivrea diorite (Bigioggero *et al.* 1979);
(iii) the sediments have the bulk composition of the Tre Valli Bresciane micaschist (Origoni & Gregnanin 1983).

For each bulk composition, Perple$_X$ produced 10 000 different densities for temperatures between 300 and 1600 K and pressures between 0 and 7 GPa (Borghesan 2011 and Fig. C2), and each density has been linked to different *p–T* conditions predicted by the models. In this way, the variations in density inside the oceanic crust, the continental crust and the sediments are nearly continuous in relation to variations in the *p–T* conditions (Fig. C2). At each time step we iterate between the density and the pressure, driving the density changes due to phase change.

Phase changes have a dual effect, determining a variation in density and release or absorption of latent heat. However, in our models, we did not include in eq. (3) the latent heat produced by phase changes occurring in the continental and oceanic crust, by phase changes related to hydration of the mantle wedge and by phase changes regarding the transformation of the olivine in the deep mantle. Afonso & Zlotnik (2011) demonstrated that the impact of the crustal metamorphic reactions on the local thermal state is on the order of 5–10 °C, and then, the latent heat produced by phase changes of the crust can be ignored in large-scale models. Regarding the phase changes in the mantle wedge, the latent heat of serpentinization can be neglected because it is balanced at large scales by the latent heat produced by de-serpentinization (Perez-Gussinye & Reston 2001; Rupke *et al.* 2004, 2013). In addition, the influence of latent heating should laterally impact the dehydration fronts, with a slight impact on the width and on the mechanisms related to the hydrated area, such as the erosion of the upper plate and the activation of a small-scale convective flow (Arcay *et al.* 2005; Yamato *et al.* 2007). The main phase transformations occurring in the upper mantle regard the olivine (Mg, Fe)$_2$SiO$_4$, which transforms from the $\alpha - phase$ to the high-pressure polymorphs wadsleyite ($\beta - phase$) and ringwoodite ($\gamma - phase$). These reactions, such as the olivine-wadsleyite phase transition, can increase the local temperature up to 60–70 °C (van Hunen *et al.* 2001; Afonso & Zlotnik 2011); however, Negredo *et al.* (2004) observed that the introduction of the latent heat in thermal models determines a variation in the maximum depth reach by the $\alpha - phase$ of less than 50 km inside the slab, while no differences have been observed outside the slab. Moreover, Blom (2016) observed that the latent heat produced at the olivine $\rightarrow$ wadsleyite transformation is one order of magnitude smaller than the shear heating and two orders of magnitude smaller than the adiabatic heating. Thus, the effects of the introduction of the latent heat can be considered negligible for what concerns the large-scale dynamics of the upper mantle and the Bouguer gravity anomalies corresponding to the subduction zone.
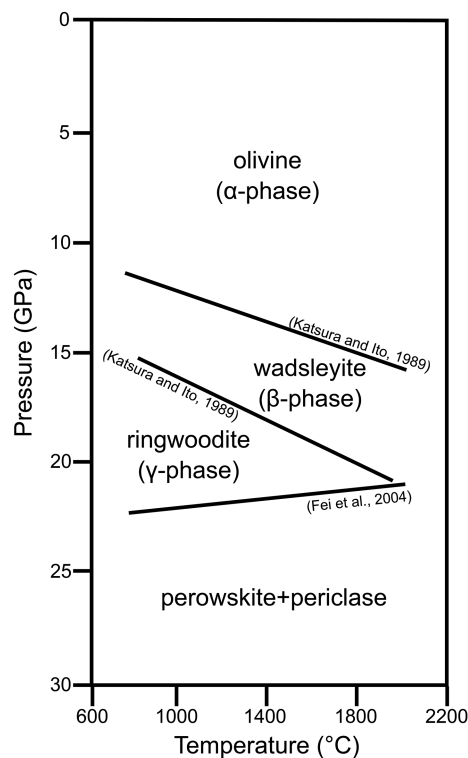

Figure C1. Stability fields of olivine (α), wadsleyite (β), ringwoodite (γ) and perovskite+periclase in isochemical peridotitic mantle. Based on Katsura & Ito (1989) and Fei *et al.* (2004).
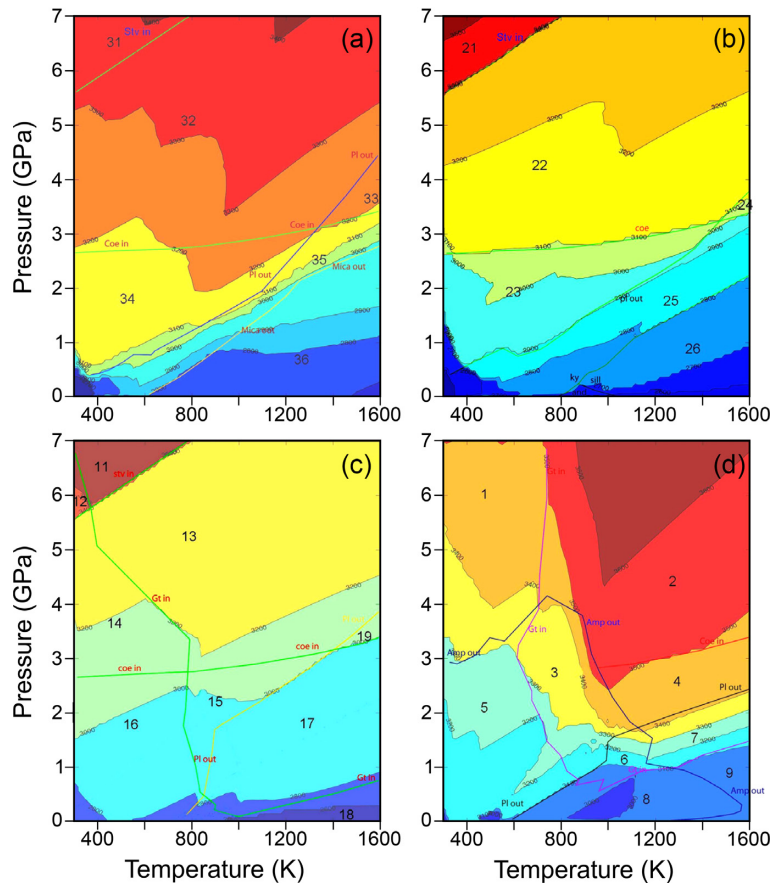
Figure C2. Density contours related to phase changes in the (a) lower continental crust; (b) upper continental crust; (c) sediments and (d) oceanic crust. Gt, garnet; Amp, amphibole; Coe, coesite; Pl, plagioclase; Stv, stishovite; Ky, kyanite; Sill, sillimanite; And, andalusite; Mica, mica (from Borghesan 2011).

APPENDIX D: COUPLING FACTOR TECHNIQUE

To implement the degree of coupling, we started from the classic *split node* technique, which allows for each node belonging to the discontinuity plane to be assigned of two different velocities, depending on the element to which it belongs. The *split node* technique, originally introduced by Jungels (1973) and Jungels & Frazier (1973) for elastic rheology, is a method used to introduce a discontinuity in the displacement/velocity along fault planes within numerical computations based on the FE method. Normally, the displacement/velocity at nodes shared by more than one element is the same for each element. The *split nodes* are special nodes in which the displacement/velocity is different depending on the element it belongs to. In this way, a generic differential slip/slip-rate $+\Delta u$ can be assigned to a node when referring to the element on one side of the fault, while a differential slip/slip-rate $-\Delta u$ is assigned to the same node when referring to the element on the other side of the faults (yellow circles in panel b of Fig. 2). The fault is thus defined by a line of split nodes. This technique is implemented locally, thus simplifying the introduction of split nodes and the assembly of the vector of the charges and the stiffness matrix, and no degree of freedom is added to the nodes (Melosh & Raefsky 1981). The original formulation of the *split node* technique, however, has not been found suitable for our modelling because it requires that the slip/slip-rate is known *a priori*. In our case, it is not possible to know *a priori* the amount of slip rate along the fault plane, leading to the results from the self-consistent thermomechanical evolution of the model.

We have modified the original formulation of the *split node* technique by introducing a coupling factor c_f that varies from 0 to 1 and indicates the percentage difference between the velocities at the two *split nodes* in such a way that

$$u_r = c_f \cdot u_l, \tag{D1}$$

where u_l and u_r are the velocities of the same *split node* belonging to the left and right elements, respectively (Fig. 2). Unlike the classical *split node* technique, which only involves modifying the load vector, this new technique also requires modification of the stiffness matrix.

Considering the two quadratic triangular elements of Fig. D1 and assuming that 1 of the 6 nodes is a *split node*, namely, node k (red circle in Fig. D1) with a coupling factor $c_f(k)$ different from 1. The velocity calculated in node k is equal to $u(k)$ when node k is considered to belong to the left element e_l, while it is equal to $c_f(k) \cdot u(k)$ when node k is considered to belong to the right element e_r. To simplify the implementation of the new technique, we define a coupling factor to all the nodes of the numerical grid, and we initialize the array with the default value equal to 1. For the *slip node*, the value of the coupling factor changes into the actual value only when the *slip node* is treated as belonging to the right element. Its value remains unchanged when the same *slip node* is treated as belonging to the left element.
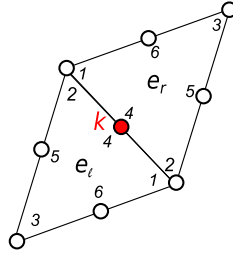
Figure D1. Scheme used to implement the modified *slip node* technique.

Following the standard formulation of the FE method, at the local scale of each element, the expression $\boldsymbol{K}^e \cdot \boldsymbol{u}^e = \boldsymbol{F}^e$ becomes:

$$
\begin{bmatrix}
K_{11} & K_{12} & K_{13} & K_{14} & K_{15} & K_{16} \\
K_{21} & K_{22} & K_{23} & K_{24} & K_{25} & K_{26} \\
K_{31} & K_{32} & K_{33} & K_{34} & K_{35} & K_{36} \\
K_{41} & K_{42} & K_{43} & K_{44} & K_{45} & K_{46} \\
K_{51} & K_{52} & K_{53} & K_{54} & K_{55} & K_{56} \\
K_{61} & K_{62} & K_{63} & K_{64} & K_{65} & K_{66}
\end{bmatrix}^e
\cdot
\begin{bmatrix}
u(1) \cdot c_f(1) \\
u(2) \cdot c_f(2) \\
u(3) \cdot c_f(3) \\
u(4) \cdot c_f(4) \\
u(5) \cdot c_f(5) \\
u(6) \cdot c_f(6)
\end{bmatrix}^e
=
\begin{bmatrix}
F(1) \\
F(2) \\
F(3) \\
F(4) \\
F(5) \\
F(6)
\end{bmatrix}^e ,
\tag{D2}
$$

where $\boldsymbol{K}^e$ is the element stiffness matrix, $\boldsymbol{u}^e$ is the vector of the element nodal displacement and $\boldsymbol{F}^e$ is the vector of the element generalized nodal forces.

After a few mathematical steps, eq. (D2) becomes:

$$
\begin{bmatrix}
K_{11} \cdot c_f(1) & K_{12} \cdot c_f(2) & K_{13} \cdot c_f(3) & K_{14} \cdot c_f(4) & K_{15} \cdot c_f(5) & K_{16} \cdot c_f(6) \\
K_{21} \cdot c_f(1) & K_{22} \cdot c_f(2) & K_{23} \cdot c_f(3) & K_{24} \cdot c_f(4) & K_{25} \cdot c_f(5) & K_{26} \cdot c_f(6) \\
K_{31} \cdot c_f(1) & K_{32} \cdot c_f(2) & K_{33} \cdot c_f(3) & K_{34} \cdot c_f(4) & K_{35} \cdot c_f(5) & K_{36} \cdot c_f(6) \\
K_{41} \cdot c_f(1) & K_{42} \cdot c_f(2) & K_{43} \cdot c_f(3) & K_{44} \cdot c_f(4) & K_{45} \cdot c_f(5) & K_{46} \cdot c_f(6) \\
K_{51} \cdot c_f(1) & K_{52} \cdot c_f(2) & K_{53} \cdot c_f(3) & K_{54} \cdot c_f(4) & K_{55} \cdot c_f(5) & K_{56} \cdot c_f(6) \\
K_{61} \cdot c_f(1) & K_{62} \cdot c_f(2) & K_{63} \cdot c_f(3) & K_{64} \cdot c_f(4) & K_{65} \cdot c_f(5) & K_{66} \cdot c_f(6)
\end{bmatrix}^e
\cdot
\begin{bmatrix}
u(1) \\
u(2) \\
u(3) \\
u(4) \\
u(5) \\
u(6)
\end{bmatrix}^e
=
\begin{bmatrix}
F(1) \\
F(2) \\
F(3) \\
F(4) \\
F(5) \\
F(6)
\end{bmatrix}^e .
\tag{D3}
$$